Aerosol Dynamics: Applications in Respiratory Drug Delivery

by

Emadeddin Javaheri

A thesis submitted in partial fulfillment of the requirements for the degree of

Doctor of Philosophy

Department of Mechanical Engineering

University of Alberta

Abstract

This study comprises four integral parts. Each part focuses on one aspect of the general problem of drug delivery by respiration. The morphological features of human respiratory tract, the dynamics of inhaled pharmaceutical particles, and the mechanics of inhaler devices are particularly taken into consideration.

In the first part, an idealized geometry of the infant nasal airways is developed with the goal of mimicking the average inertial filtration of aerosols by the nasal passages. Paramount geometrical features of 10 previously published nasal replicas of infants aged 3–18 months have been considered in creating the idealized version. A series of overall deposition measurements have been carried out in the idealized replica over a range of particle sizes and breathing patterns. A satisfactory agreement was observed between deposition data for the idealized geometry and those from 10 in vitro subjects.

In the second part, the effect of using helium–oxygen mixture instead of air on hygroscopic size change of inhaled droplets is investigated, with the focus on the favorable transport properties of helium-oxygen. Initially isotonic saline droplets with lognormal size distribution are considered. The effect of mass fraction of the inhaled droplets is highlighted. For high mass fraction, evaporation of smaller droplets saturates the carrier gas, and prevents the evaporation of larger droplets, so hygroscopic effects are believed to be of marginal importance regardless of the carrier gas. In contrast, for medium and low mass fractions, the carrier gas remains less affected by the dispersed phase, and larger droplets are more likely to shrink and pass through the upper airways. In this case, the effects of the physical properties of the carrier gas are more pronounced.

In the third part, the problem of hygroscopic size change of nebulized aerosols is considered, and two approaches to size manipulation of saline droplets are investigated. First, heating the aerosol stream, and second, adding solid sodium-chloride particles to the aerosol stream. The two approaches are aimed at altering the vapor pressure balance between the surface of the droplets and their carrier gas. These processes help the droplets which are larger than optimal to evaporate and shrink, thereby producing desirable droplets for drug delivery, which have less deposition in the extra-thoracic airways and more deposition in the alveolar region of the lung.

In the fourth part, the dynamic equation for the flocculation and upward drift of the suspended drug particles within the canister of a metered dose inhaler is solved numerically. The technique employed is based upon discretizing the particle size distribution using orthogonal collocation on finite elements. This is combined with a finite difference discretization of the canister geometry in the axial direction, and an explicit Runge-Kutta-Fehlberg time marching scheme. The solution represents the particle size distribution as a function of time and position within the canister. The method allows prediction of the effects of the initial conditions and physical properties of the suspension on its dynamic behavior and phase separation.

Preface

This thesis is an original work by Emadeddin Javaheri. Chapter 2 of this thesis has been published as E. Javaheri, L. Golshahi, and W.H. Finlay, 2013. "An idealized geometry that mimics average infant nasal airway deposition," Journal of Aerosol Science, vol. 55, 137–148. I was responsible for the development of the idealized geometry as well as the manuscript composition. L. Golshahi assisted in measuring deposition of particles in the geometry, and contributed to manuscript edits.

Chapter 3 of this thesis has been published as E. Javaheri, F.M. Shemirani, M. Pichelin, I.M. Katz, G. Caillibotte, R. Vehring, and W.H. Finlay, 2013. "Deposition modeling of hygroscopic saline aerosols in the human respiratory tract: Comparison between air and helium–oxygen as carrier gases," Journal of Aerosol Science, vol. 64, 81–93. I was responsible for the numerical simulation (developing a computational code) as well as the manuscript composition. F.M. Shemirani assisted in measuring deposition of stable particles inhaled with helium–oxygen, and contributed to manuscript edits. M. Pichelin, I.M. Katz, G. Caillibotte, and R. Vehring were all involved with concept formation, and also helped edit and revise the manuscript.

Chapter 4 of this thesis has been published as E. Javaheri, and W.H. Finlay, 2013. "Size manipulation of hygroscopic saline droplets: Application to respiratory drug delivery," International Journal of Heat and Mass Transfer, vol. 67, 690–695. I was responsible for the numerical simulation (developing a computational code) as well as the manuscript composition.

Chapter 5 of this thesis has been published as E. Javaheri, and W.H. Finlay, 2014. "Numerical simulation of flocculation and transport of suspended particles: Application to metered-dose inhalers," International Journal of Multiphase Flow, vol. 64, 28–34. I was responsible for the numerical simulation (developing a computational code) as well as the manuscript composition.

In all the aforementioned publications W.H. Finlay was the supervisory author and was involved with concept formation and manuscript composition.

Dedication

To my beloved wife Sara

Acknowledgement

I would like to express my deepest appreciation to my supervisor Professor Dr. Warren H. Finlay, you have been a tremendous mentor for me. I would like to thank you for encouraging my research, and also for your supportive attitude. Without your supervision and constant help this dissertation would not have been possible. A special thanks to Dr. Reinhard Vehring for valuable discussions and useful suggestions, and to Dr. Carlos Lange for serving as my committee member.

Contents

List of Tables

List of Figures

1. Introduction

The material of this thesis is organized in four parts, contained in chapters 2 to 5. Each part tackles a challenge in respiratory drug delivery.

In the second Chapter, an idealized geometry is developed that mimics the average deposition of micrometer-sized particles in the extrathoracic nasal airways of human infant. The extrathoracic airways behave somewhat like a coarse filter during inhalation of aerosol particles. However, morphological aspects strongly affect the characteristics of deposition in these airways. These aspects depend on the age, gender, race, health and certain physical features. Measured deposition data are scattered over a wide range due to inter-subject variability (Stahlhofen et al., 1989). Efforts have been made to eliminate or decrease the effect of inter-subject variability on the deposition data and collapse the data points on a single plot (Cheng, 2003; Storey-Bishoff et al., 2008; Garcia et al., 2009; Golshahi et al., 2010).

Of particular interest is the deposition of micrometer-sized pharmaceutical and environmental toxic aerosols in the upper airways. For particle sizes larger than approximately a half micrometer, this is controlled by inertial impaction (Cheng, 2003), and is traditionally reported via the impaction parameter $d_a^2\,Q$ where d_a is the aerodynamic diameter and Q is the volume flow rate (Yu et al., 1981). Although this form of impaction parameter is widely accepted, it does not collapse the scattered data, even for a single subject (Stahlhofen et al., 1989).

Pressure drop across the airway depends on the mass flow rate as well as the shape and size of the airway. Thus, if pressure drop is included in the impaction parameter, these factors will be indirectly considered. In this way, $d_a^2\,\Delta p$ originally suggested by Hounam et al. (1971), could be used as an impaction-related parameter. While pressure drop is not available for most existing deposition studies, Storey-Bishoff et al. (2008); Garcia et al. (2009); Golshahi et al. (2010, 2011) found that inclusion of pressure drop in an inertial parameter did appreciably reduce the scatter of deposition data in child nasal airways.

Another alternative for impaction parameter, which may effectively decrease the effects of inter-subject variability, is a combination of Reynolds and Stokes dimensionless numbers in the form $Re^{\alpha}\,Stk^{\beta}$. In defining Reynolds and Stokes numbers, a length scale must be specified. While the choice of length scale depends on the shape of the airway, for the oral airway, which is quasi-circular in many cross sections, Grgic et al. (2004a) found that the square root of the volume over the length of the airway provides an excellent collapse of oral deposition data. For the nasal airway, Swift (1991) used the cross sectional area at the site of maximum velocity (the nasal valve) to determine the length scale.

To further collapse inter-subject variability, one may plot deposition data vs. an impaction parameter containing Reynolds and Stokes numbers as well as a length scale of the airway. In other words, an extra geometric factor, beyond Reynolds and Stokes numbers, could be considered. This length scale also depends on the shape of the airway, and should be similar to that which is used in definition of Reynolds and Stokes numbers. Storey-Bishoff et al. (2008) found that airway volume divided by airway surface area best collapses the deposition data in infant nasal airways for micrometer- sized particles.

All the aforementioned approaches can reduce the scatter of data to some extent. However, as long as one deals with several subjects or replicas, deposition data cannot be collapsed exactly onto a single unique characteristic curve. An alternative paradigm is to construct a representative idealized airway to capture average deposition. Regarding the effects of passage geometry, there are some cardinal features that dominate deposition. Once these features are captured in a unique geometry, the deposition characteristic for such geometry could be considered as an average representation of the real airways. This stimulates development of simplified idealized geometries for particular segments of the respiratory tract.

The idealized adult oral airway of Stapleton and Finlay (1997) exemplifies the possibility of developing idealized airways. This model is widely accepted and applied as typical of oral airway geometries and its utility in the study of the pharmaceutical aerosol administration is well established (Stapleton et al., 2000; DeHaan and Finlay, 2001; Grgic et al., 2004b; Wang et al., 2006; Brouns et al., 2007; Coates et al., 2007; Jin et al., 2007; Mitsakou et al., 2007; Zhang et al., 2007; Zhou et al., 2011).

The second Chapter is aimed at developing an idealized geometry for infant nasal airways. Considering the existence of several realistic replicas as well as their corresponding deposition data (Swift, 1991; Cheng et al., 1995; Janssens et al., 2001; Mitchell, 2008; Storey-Bishoff et al., 2008; Laube et al., 2010), constructing a new idealized model for infant nasal airway is attractive. The importance of studying the infant nasal geometry is underlined by the fact that infants tend to breathe through the nose more than other age groups, partly because this facilitates breathing while breast feeding. (Sasaki et al., 1977; Becquemin et al., 1991; Amirav and Newhouse, 2012). Furthermore, in vitro deposition measurements in realistic airways neces-

sitate using computed tomography scans, which produce harmful radiation, and especially for the case of infants, should be performed only when absolutely necessary. This may be considered as a further advantage of an idealized geometry as a reference airway model.

Developing an idealized geometry is inherently a heuristic task, i.e., no standard algorithm exists for producing an idealized version representing a number of real geometries. In fact, design of an idealized geometry is a compromise between simplicity and exactness. A possible strategy is to explore many subjects, and calculate a generalized average for each cross section, and build the average geometry based on the average cross sections (Liu et al., 2009). Such an idealized geometry can mimic average deposition in the real subjects, but, due to its complicated cross sections, it is difficult or impossible to manufacture using inexpensive, readily available methods that would be amenable to specification in pharmacopeial standards. An alternative strategy, which is adopted in the second Chapter, is to simplify the features which do not significantly influence particle deposition but make the geometry unnecessarily convoluted.

In order to address the paramount geometrical characteristics of infant nasal airways, which dominate trans-nasal particle impaction, a simplified idealized geometry is developed, thereby providing a reference model to study the inertial filtration effects of the infant nasal passage. Deposition measurements, for different breathing patterns and particle sizes, are conducted to ensure that the deposition characteristics of the idealized airway agree with the average of the in vitro inertial deposition data provided by Storey-Bishoff et al. (2008).

The third Chapter deals with hygroscopic size change of inhaled droplets, and

underlines the effects of thermodynamic and transport properties of carrier gas on these size changes.

The particle diameters of inhaled hygroscopic aerosols can change due to evaporation and condensation. This results in transfer of heat and vapor between the particles or droplets and the surrounding gas. The driving force of this process is the vapor concentration difference between the particle or droplet surface and the bulk gas. Either volatile droplets or initially solid hygroscopic particles may experience size changes. Volatile droplets evaporate and shrink because of high vapor concentration at the immediate vicinity of their surface (Persons et al., 1987; Chan et al., 1994; Phipps and Gonda, 1994; Finlay and Stapleton, 1995; Finlay et al., 1996; Finlay, 1998). Hygroscopic particles can instead undergo condensational growth by absorbing vapor from nearly saturated air in the respiratory passages (Martonen, 1982; Broday and Georgopoulos, 2001; Londahl et al., 2007; Longest and Xi, 2008; Hindle and Longest, 2012).

When hygroscopic droplets are inspired, the shrinkage or growth as well as the rate of approach to thermodynamic equilibrium between droplets and the carrier gas are influenced by the physical properties of the gas. In pharmaceutical aerosol applications, evaporation of drug-containing droplets could be beneficial because this can lead to smaller droplet sizes during passage through the upper airways, thereby reducing unwanted extra-thoracic deposition. This points to the use of alternative gases with more favorable transport properties than air.

A helium-oxygen mixture is a low density gas with potential advantages in inhalation therapy (Svartengren et al., 1989; Habib et al., 1999; Goode et al., 2001; Corcoran and Gamard, 2004), particularly for treating patients with severely ob-

structed airways. When drug particles are carried by helium-oxygen, unwanted deposition in delivery devices decreases (Corcoran et al., 2003). Helium-oxygen can also lessen undesirable ex vivo losses of aerosol associated with deposition in breathing supply circuitry with ventilated patients (Goode et al., 2001; Dhand, 2004). Furthermore, when particles are inspired with helium-oxygen, deposition in the extra-thoracic airways decreases (Gemci et al., 2003; Darquenne and Prisk, 2004; Peterson et al., 2008); Thus, higher deposition in the lung is expected. The role of helium-oxygen in respiratory medicine, and the relation between its potential effects and physical properties has been reviewed by Ari and Fink (2010). Recently, Conway et al. (2012) have conducted *in-vivo* deposition measurements which include both air and helium-oxygen as carrier gases. Because of the high mass fraction of droplets, hygroscopic effects are deemed to be insignificant in that study.

The present work focuses instead on hygroscopic effects when helium-oxygen mixture is the carrier gas. Shrinkage and growth of droplets can be mathematically modeled using simplified hygroscopic theory (Fuchs, 1959; Mason, 2010). Earlier models do not account for the effects the droplets have on the surrounding gas (Persons et al., 1987; Ferron et al., 1988-b; Stapleton et al., 1994). However, transfer of vapor and heat from the surface of the dispersed droplets may considerably change the temperature and moisture content of the gas. In realistic situations, the final temperature and humidity of the gas could determine the state of equilibrium. A more advanced approach is to consider two way coupling in which the thermodynamic state of the gas may change due to heat and vapor exchange with the dispersed droplets (Finlay and Stapleton, 1995; Longest and Hindle, 2010).

The present study examines the behavior of initially isotonic hygroscopic aerosols inhaled into the respiratory tract by applying the methodology provided by Finlay

and Stapleton (1995) with several modifications to allow consideration of helium-oxygen. These modifications include calculation of the coefficients of heat and vapor transfer between the carrier gas and the airway walls using computational fluid dynamics simulations in the Alberta idealized upper airway geometry. In addition, a recently developed dimensionless correlation (Golshahi et al., 2013) for extra-thoracic deposition during tidal breathing is used. The results allow comparison of the behavior of inhaled hygroscopic aerosols when helium-oxygen *vs.* air is used as the carrier gas.

The fourth Chapter introduces two approaches to controlled evaporation of nebulized volatile droplets. Nebulizers are inhaler devices that provide therapeutic materials in the form of aqueous solution aerosols. However, the size of some nebulized droplets is not necessarily optimal for drug delivery to the lungs (O'Callaghan and Barry, 1997; Nerbrink and Dahlbäck, 1994). Fortunately, smaller droplets can be obtained by evaporation. The driving force for the evaporation of the aqueous droplets is the gradient of vapor concentration between the vicinity of the droplet surface and the surrounding air. Therefore, when the temperature and relative humidity (RH) at the surface of droplet equal those of the surrounding air, evaporation does not take place. Nevertheless, increasing the temperature of the dispersed droplets, or decreasing the moisture content of the continuous phase can trigger evaporation. When an aerosol stream is heated, the vapor concentration at the surface of the droplets rapidly increases, e.g. the concentration of water vapor at the flat surface of liquid water at 15°C is 12.9 g/m^3 while at 30°C it is 30.2 g/m^3 (Seinfeld and Pandis, 2006). This is a familiar concept in heating ventilation and air-conditioning (HVAC) applications and also could be used to adjust the size dis-

tribution of aqueous aerosols. Throughout the present study, heating the aerosol stream will be referred to as the HA approach.

A different way to trigger the evaporation of droplets is to remove water vapor from the carrier air. This could be performed by adding excipient salt (e.g. sodium chloride) particles to the aerosol stream. These particles absorb the water vapor and undergo condensational growth. As a consequence, vapor concentration in the bulk air decreases and the original saline droplets start to evaporate. Adding excipient particles to the aerosol stream will be referred to as the EA approach. This was first developed by Longest and Hindle (2011, 2012).

Alternative size manipulation approaches consider creating submicrometer particles which effectively pass through the extrathoracic airways, and then increasing the aerosol size in the thoracic airways to prevent exhalation of the particles. This may be accomplished by combining the aerosol stream with saturated or supersaturated air stream a few degrees above body temperature, or by creating initially submicrometer particles containing both drug and a hygroscopic excipient. The former is referred to as the Enhanced Condensational Growth (ECG) (Hindle and Longest, 2010), and the latter as the Excipient Enhanced Growth (EEG) (Longest et al., 2012b).

Hygroscopic size changes are accompanied by transfer of mass and heat between the dispersed droplets and their surrounding air. This yields changes in temperature and moisture content of the air, i.e. the mass and heat transfer between the phases are two-way coupled. The higher the mass concentration of the dispersed droplets, the higher the influence on the surrounding air. Shrinkage and growth of droplets can be mathematically modeled using simplified hygroscopic theory (Fuchs, 1959;

Mason, 2010). Two way coupling can be also modeled using the approach of Finlay and Stapleton (1995). Subsequent to size manipulation, saline droplets will be inspired. They will continue their size changes during progress through the respiratory airways. Regional deposition of these size varying droplets can be predicted using the approach of Finlay and Stapleton (1995) and Javaheri et al. (2013b).

Chapter 4 focuses on the dynamics of droplet shrinkage during the HA and EA processes, prior to inspiration. The shrunk droplets are supposed to penetrate deeper into the lung. This is examined using the approach given by Javaheri et al. (2013b).

The fifth Chapter introduces a numerical approach to simulate flocculation and convective transport of drug particles suspended in a liquid propellant, within the canister of a pressurized metered-dose inhaler (MDI), the most commonly used device for respiratory drug delivery (Hickey and Evans, 1996; Finlay, 2001). Within the canister of an MDI, drug is either dissolved or colloidally suspended in a liquid propellant. The latter is the subject of Chapter 5. The ability of a drug-propellant suspension to remain in its original state, i.e. its stability, is critical because any change may interfere with the consistency of the drug delivery. Such changes may include any variation in the drug particle size distribution, and any macroscopic transport of the particulate phase. Inter-particle collisions and floc formation can alter the particle size distribution. Relative motion of the dispersed particles, as well as their natural tendency to decrease the large specific surface area may give rise to collisions. Thus, a proclivity towards instability is inherent in many suspensions. However, whether or not particles collide and flocculate is determined by inter-particle forces.

In colloidal systems, inter-particle forces are usually described by the DLVO[1] theory (Derjaguin and Landau, 1941; Verwey and Overbeek, 1948). Two types of particle interactions are considered in this theory: attractive van der Waals force, and repulsive electrostatic force due to the presence of electrical double layers. Dominance of the repulsive force gives rise to stability, and dominance of the attractive force causes flocculation and instability. However, in non-aqueous liquids with low conductivity and low dielectric constant, like propellants, the repulsive forces are thought to be trivial, mainly because of the insignificance of the electrical double layer (Albers and Overbeek, 1959a,b; Chen and Levine, 1973; Féat and Levine, 1975, 1976; Johnson, 1996). Thus the electrostatic repulsion is presumed to be negligible in the present study, and under the dominance of the van der Waals force, the evolution of an unstable suspension from an arbitrary initial condition is considered.

The van der Waals force, however, is a short range force and decays rapidly to zero away from the surface of the particle. In fact, within the MDI canister, particle collision frequency is controlled by two other mechanisms: upward velocity differential and Brownian motion, and the van der Waals force indeed enhances these mechanisms.

Simultaneous with flocculation, particles drift upward or sediment under the effect of gravity. Without reducing generality, only the case in which the true density of particles is lower than that of propellant, and particles drift upward, is presented here.

In the present study, flocculation is modeled via the continuous form of the particle number balance equation of Smoluchowski (Chandrasekhar, 1943; Fried-

[1]Derjaguin-Landau-Verwey-Overbeek

lander, 2000; Benjamin, 2011), and the upward transport of the particulate phase is described by a convection term. The overall mathematical model is a nonlinear transient partial integro-differential equation, which is a reduced form of the general dynamic equation (GDE) of aerosols (Gelbard and Seinfeld, 1979; Williams and Loyalka, 1991; Friedlander, 2000). In reality, the GDE takes many and various forms, which typically must be solved numerically. Because of the variety of the mathematical terms which may appear in the GDE, there is no generally accepted numerical solution approach. Some classic numerical work on discrete and continuous forms of the GDE is reported by Gelbard (1979). In the present form of the GDE, flocculation is the challenging term. Several numerical approaches have been established to analyze flocculation, including orthogonal collocation on finite elements (Gelbard and Seinfeld, 1978), cubic splines (Gelbard and Seinfeld, 1978; Gelbard et al., 1980), sectional representation (Gelbard et al., 1980), modal aerosol dynamic model (Whitby and McMurry, 1997), to mention a few. A comparative review of algorithms used to simulate aerosol dynamics is given by Williams and Loyalka (Williams and Loyalka, 1991) and also by Zhang et al (Zhang et al., 1999). The method of orthogonal collocation on finite elements (Gelbard and Seinfeld, 1978; Carey and Finlayson, 1975; De Boor and Swartz, 1973; Douglas and Dupont, 1973) is used here.

From a particle interaction point of view, the system under consideration is inherently unstable. The consequence of instability is phase separation into a concentrated particulate phase and a dilute propellant. The goal of the present simulation is to predict the state of the system, i.e. the particle size distribution as a function of time and position, and to calculate a characteristic time of phase separation.

2. An idealized geometry that mimics average infant nasal airway deposition

2.1 Introduction

Inter-subject biological variability, due to shape and size differences, is one of the most challenging aspects in the study of aerosol deposition in the extrathoracic respiratory passages. An idealized geometry of the infant nasal airways is developed in this Chapter, with the goal of mimicking the average inertial filtration of aerosols by the nasal passages, thereby providing a reference model for aerosol deposition studies (Javaheri et al., 2013a). Paramount geometrical features of 10 previously published nasal replicas of infants aged 3–18 months (Storey-Bishoff et al., 2008) are considered in creating the idealized version. Simplifications are made to features that do not significantly influence deposition but that make the airway unnecessarily convoluted. A series of overall deposition measurements have been carried out in the idealized replica over a range of particle sizes and breathing patterns. Deposition data for the idealized geometry are compared with those from 10 in vitro subjects. Satisfactory agreement between deposition in the idealized and real geometries suggests that the idealized version can characterize average deposition in the real airways. The present idealized airway could be useful as a reference geom-

etry in experimental and theoretical studies of aerosol delivery through infant nasal airways.

2.2 Methods

2.2.1 Real nasal geometry

The nasal cavity is separated into two distinct airways by a vertical dividing wall termed the nasal septum. The nasal cavity is essentially symmetric about the septum, although during normal breathing, each of the two passages is preferentially used alternately for several hours at a time. Inhaled air enters the nasal airway through the nostril and then passes through the nasal valve, which is usually the narrowest part of the nose. Being the segment with minimum cross-section area, it acts as a flow limiter. The main nasal passages, with an abrupt increase in cross-sectional area, are located posterior to the nasal valve. This part of the airway is mainly shaped by the nasal septum and three projections referred to as the inferior, middle, and superior turbinates (also called the nasal conchae) (Marieb and Hoehn, 2007). One role of the turbinates is to promote local turbulent mixing. However, previous studies (Hahn et al., 1993; Keyhani et al., 1995; Schreck et al., 1993) indicate that flow in the adult nasal cavity is mostly laminar during normal resting breathing. The passages between the nasal conchae are narrower in infants, and volume flow rates are noticeably lower compared to adults. As a result, flow disturbances are damped and turbulence is unlikely. From a heat transfer point of view, turbinates are extended surfaces which crucially contribute to heat and moisture transfer from airway walls to the inhaled air. The narrow passages between the

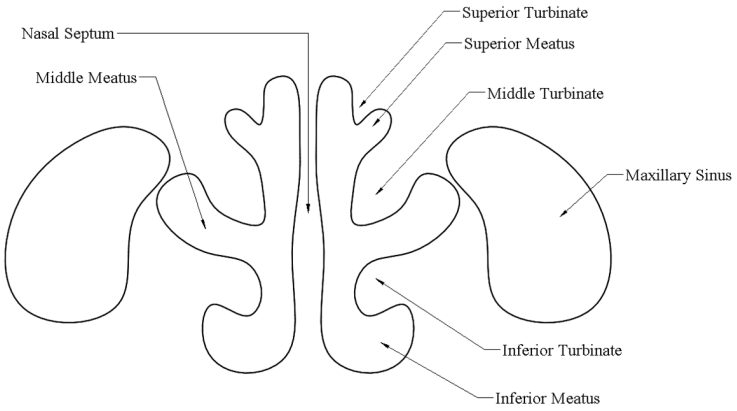

Figure 2.1: Schematic of cross section of the nasal cavity.

turbinates are called the meatus. Most inhaled airflow travels between the inferior turbinate and the middle turbinate (through the middle meatus). The maxillary sinuses lie lateral to the middle meatus. Figure 2.1 schematically illustrates a cross section of the nasal cavity, with physiological nomenclature (Proctor and Andersen, 1982).

In some subjects, particularly in infants, one or both of the maxillary sinuses and middle meatus are connected through an orifice (Storey-Bishoff et al., 2008). The inclusion of sinuses makes the geometry of this region highly convoluted. Turbinates direct the air stream into the nasopharynx. There is no separating wall in the nasopharynx, so the airflows coming from left and right nasal passages are mixed together here. From a fluid dynamics point of view, the nasopharynx is a 90 degree bend which directs air towards the larynx and trachea.

While different regions of adult and infant nasal airways can be qualitatively described in nearly the same way, the overall morphology of the infant nasal airway is quite different from that of adults. In contrast to adults, the cross section of minimum area in infant nasal airway is noticeably larger than that of the oral airway,

mainly because of the close distance between the epiglottis and palate (Amirav and Newhouse, 2012). The infant nasal airway is in some sense optimized to facilitate nose breathing. This can partially explain the anatomical differences. Partly because of these differences, effective drug delivery to infants and younger children requires special considerations (Becquemin et al., 1991; Phalen and Oldham, 2001; Bennett et al., 2008).

2.2.2 Idealized nasal geometry for infants

Deposition of micrometer-sized particles in the extrathoracic airway is dominated by inertial impaction. Impaction of particles is characterized by two dimensionless numbers that arise from a dimensional analysis of the governing equations i.e. the Reynolds and Stokes numbers. The Reynolds number is the ratio of inertial fluid forces to viscous fluid forces. The Stokes number is the ratio of stopping distance of a particle in the flow to a characteristic length in the geometry. The deviation of particles from curved streamlines is of order of magnitude given by their stopping distance. Thus, the higher the Stokes number the more the probability of deposition. As a general rule, all geometrical features that bend the streamlines may cause the particles to deviate from them, thereby depositing on the airway walls. Therefore, such features should be taken into consideration in the idealized model.

We started our design by extensively exploring the nasal geometries of 10 infants aged 3–18 months. The geometries were obtained by Storey-Bishoff et al. (2008) from computed tomography (CT) scans of seven male and three female infants. These CT scan images had been used subsequently by Storey-Bishoff et al. (2008) for preparing STL files, fabricating the nasal passage replicas, and measuring deposition

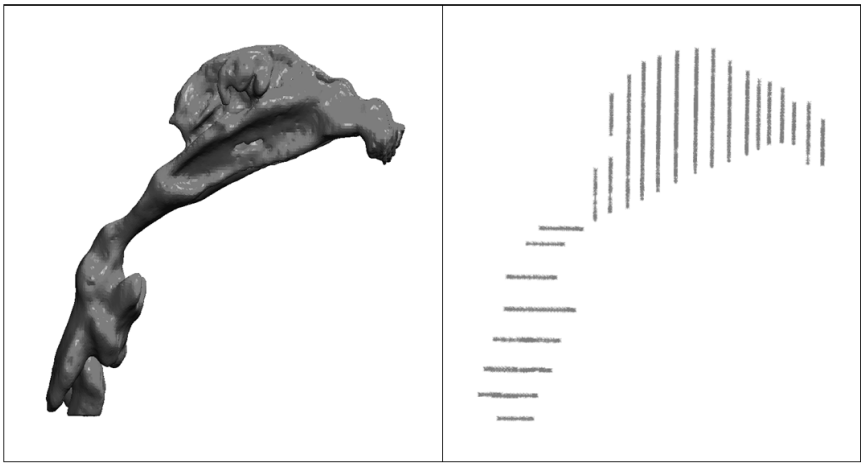

Figure 2.2: Placement of the 24 cross sections on a real airway.

of micrometer-sized particles in them.

In order to create the idealized geometry, cross sections of different regions of the real airways and face were surveyed using ScanTo3D (SolidWorks Premium, Dassault Systemes). The previously prepared digitized data were imported into SolidWorks in the form of STL files. Cross-sectional curves on the point cloud data were created, and then used as reference to build a parametric model. In an attempt to determine the primary features of the real geometries, and design the idealized version, 24 cross sections of each subject were explored. Segments with more complexity were surveyed using preferentially more cross sections. Figure 2.2 shows the placement of the 24 cross sections on a real airway.

Care was taken to maintain the primary features. Idealized cross sections were created with the aid of two dimensional splines, and the idealized airway took shape based on these cross sections. SolidWorks uses non-uniform rational basis spline (NURBS), which is a generalization of both B-spline and Bezier curve and is commonly used in computer-aided- design (CAD) software. See Lombard (2008) for a

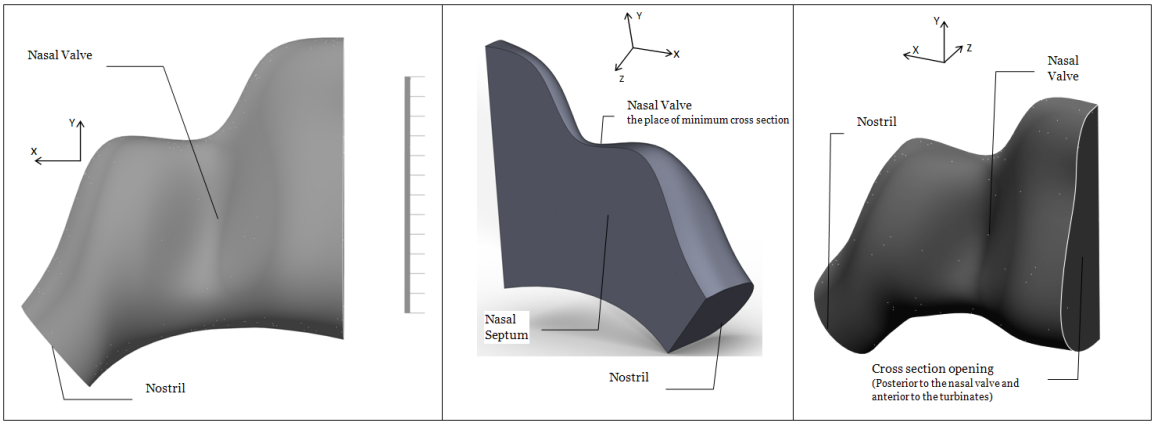

Figure 2.3: Proximal region of the idealized geometry. The markings on the ruler indicate 1 mm.

complete discussion on using splines for complex shape modeling in SolidWorks.

The idealized model extends from the nostril entrance to just past the larynx. Also, the surface of the face from the chin to forehead is included. The nasal cavities are bounded medially by the nasal septum, which is a vertical cartilage. The idealized nasal septum is exactly midline, separating the left and right sides of the nose into passageways of equal size. Although a normal septum is neither off-middle nor deviated, because septum cartilage is thicker at the margins than at the center, its surface is not quite smooth. However, septum bumps do not compare in scale with the major geometrical features that form the air flow, so that deviation of the septum surface from flatness is not expected to impact the curvature of the flow streamlines. Therefore, the idealized nasal septum was created as a flat plane. The first region of the idealized nasal airway is depicted in Fig. 2.3 with three different views. This proximal region includes the nostril and the nasal valve.

As in the real airways, the turbinate region is designed to be located posterior to the nasal valve. In most of the 10 subjects, a connection between the maxillary sinus and middle meatus was observed in the form of an orifice or a narrow slit

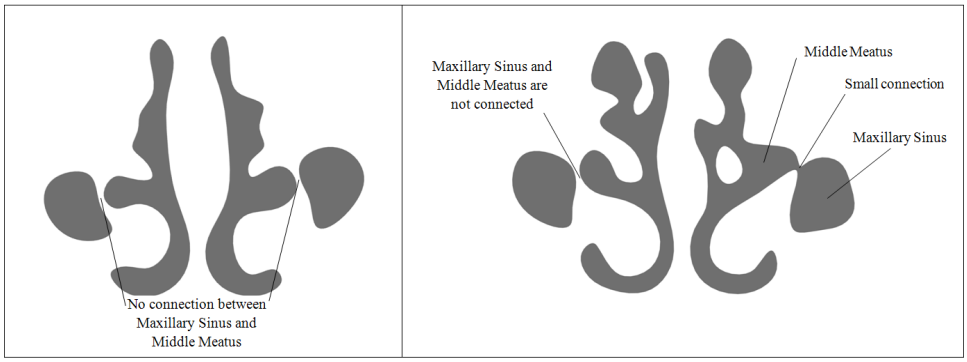

Figure 2.4: Two different cross sections from real airways in the turbinate region from the Storey-Bishoff et al. (2008) subjects: one with maxillary sinus and middle meatus not connected (left) compared to one with maxillary sinus and middle meatus connected in the left passage (right).

(see Fig. 2.4). In addition to its small opening, this connection is perpendicular to the direction of the main flow. Therefore, the effect of sinuses on normal inertial deposition was deemed to be trivial and they are excluded from the idealized airway. Figure 2.4 is the cross-sectional view of the nasal cavity in the turbinate region, for two different real replicas. This figure illustrates the possibility of interconnection between maxillary sinus and middle meatus.

Nasal conchae are projections with irregular shape. Accordingly, meatus airways, the narrow passages between nasal conchae, have irregular cross sections. Flow in these narrow airways is laminar, and the streamlines have little curvature. Thus, the irregularity of the nasal meatus is deemed not to have a marked contribution to total deposition, and they have been simplified in the idealized geometry to be airways of regular cross section. Figure 2.5 depicts the general form of the idealized nasal cavity. Sections (b) and (c) illustrate the idealized configuration of the nasal conchae and meatus airways.

The turbinate region is the region of highest geometric complexity. Distal to the

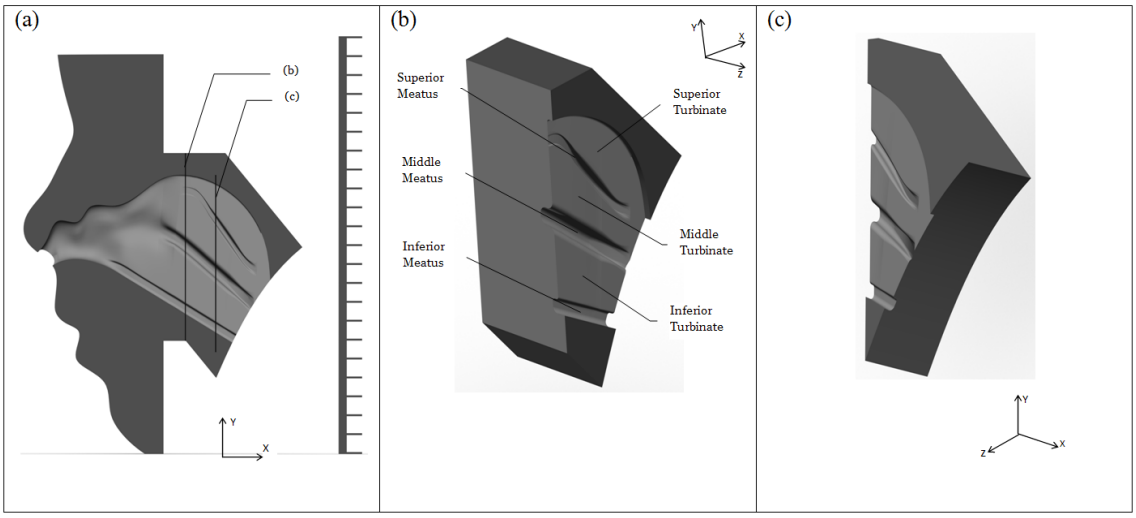

Figure 2.5: Two successive sections (b and c) of the right half of the idealized nasal cavity at locations shown in (a). The view in (a) is side-on (i.e. sagittal), while the views for (b) and (c) are from varying oblique positions as seen by the axis directions. The markings on the ruler indicate 5 mm.

turbinates, the nasal septum terminates, and airflows from left and right passages are mixed and directed to the nasopharynx. The form of the 10 real subjects in the nasopharynx and larynx regions is relatively straightforward and fewer simplifications are needed here compared to the turbinate region. In these regions, the real subjects differ mostly in size and in a few details of their shape. Figure 2.6 shows the idealized geometry in the nasopharynx and larynx regions in two different views.

The idealized geometry should possess the characteristics of real airways, not only in form but also in size. At a minimum, the characteristic dimension of the idealized geometry should be scaled to the average of that for real geometries. For a convoluted passage like a nasal airway, it is quite difficult to designate a single length scale to represent the entire geometry. However, Storey-Bishoff et al. (2008) examined a variety of length scales and found that airway volume divided by airway surface area is the single most appropriate length scale representing infant nasal

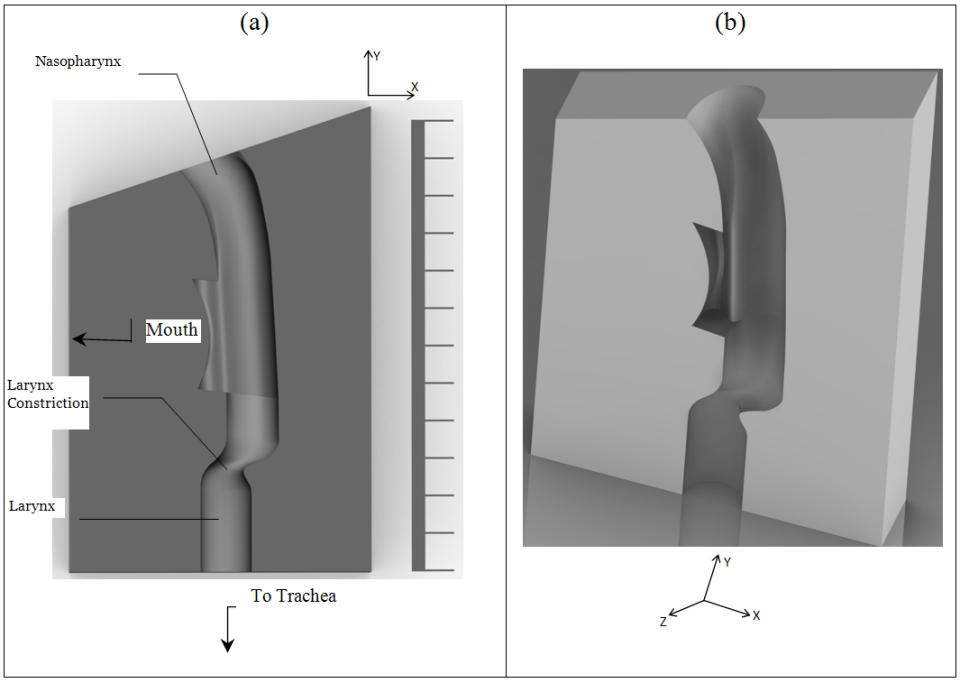

Figure 2.6: The right half of the idealized nasopharynx and larynx: (a) side-on (sagittal) view and (b) anterior oblique view as seen by the axis directions. The markings on the ruler indicate 5 mm.

	D_h (mm)	A_{min} (mm^2)	V (mm^3)	$A_s(mm^2)$
Average dimension in 10 real replicas	4.8 ± 0.74	62.25 ± 11.62	11636 ± 3210	9645 ± 1952
Dimension in the idealized replica	4.8	67.00	11445	9538

Table 2.1: Comparison of the geometrical dimensions of the idealized replica with average geometrical dimensions in 10 real replicas, given as mean ± standard deviation (n=10). Here, D_h denotes hydraulic diameter, A_{min} denotes the minimum cross sectional area taken perpendicular to expected airflow, V is the volume of the airway, and A_s is the area of the interior surface.

airway dimension as far as aerosol deposition of micrometer-sized particles is concerned. They also reported a value of 1.2 mm for the average of this length scale for their 10 replicas. This length scale is adopted in the current study with a trivial modification. In particular, to be quantitatively more sensible, the former length scale is redefined by multiplying by 4.0. This corresponds to the average hydraulic diameter for the overall airway, and its value is much closer to the actual physical airway sizes.

The present idealized geometry was scaled to have an average hydraulic diameter equal to the average value of the 10 Storey-Bishoff et al. (2008) subjects. Furthermore, to calculate the dimensionless Reynolds and Stokes numbers, the average of hydraulic diameter is considered here as the length scale for the overall airway.

Hydraulic diameter is thought to be the dimension that primarily determines the deposition. However, for the sake of comparison, the geometrical dimensions which may be considered to affect the deposition are summarized in Table 2.1.

Given that the maxillary sinuses are excluded in the idealized airway, the area of the interior surface and volume of the idealized airway are slightly less than the

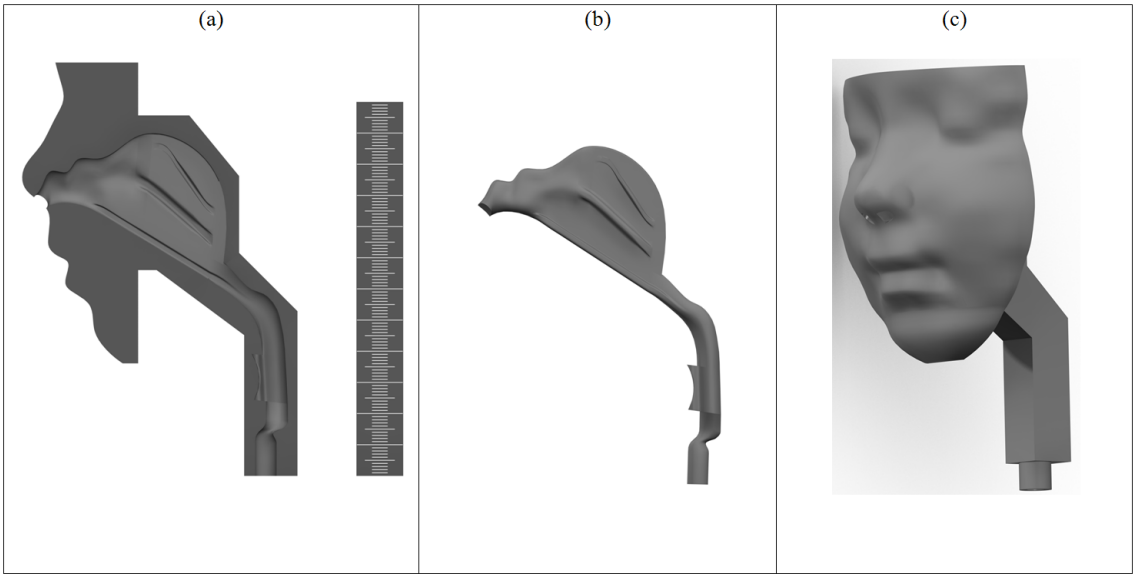

Figure 2.7: Finalized idealized infant nasal geometry: (a and b) internal airway anatomy and (c) The exterior of the replica with idealized face prepared for deposition measurements. The minor markings on the ruler indicate 1 mm.

average of the real airways. Also, the minimum cross-sectional area in the idealized geometry is just 8% more than the average. However, the average value of the hydraulic diameter in 10 realistic replicas, which is the cardinal dimension, is equal to the hydraulic diameter of the idealized airway.

Figure 2.7 depicts the final idealized internal airway geometry as well as the exterior of the model that includes an idealized face prepared for deposition measurements.

Rapid prototyping (Invision SR, 3D Systems, USA using Visijet SR200) was used to produce the idealized replica from the 3D computer model. In order to conduct the preliminary deposition measurements, we built the replica out of plastic and used jojoba oil particles for which the effect of charge is not considered to be an issue. Subsequently, to test the replica with charged particles and to conduct further complementary tests, a metal replica was built.

The roughness of the interior surfaces may considerably impact the fluid flow and deposition through the airways (Kelly et al., 2004; Schroeter et al., 2011). Deposition in the present idealized geometry is compared with those of 10 real replicas. The idealized and real replicas are all made from the same material and using the same build process; thus, in terms of surface roughness, they can be considered similar. Therefore, we do not expect any deposition discrepancy due to surface roughness differences. Previous publications have also shown good agreement with in vivo data using the present build process and materials in adults (Golshahi et al., 2011).

2.2.3 Deposition measurement

Subsequent to design and construction, deposition of micrometer-sized particles in the idealized geometry was measured. For this purpose, aerosol laden air was pulled through the replica with sinusoidal flow patterns representing tidal infant breathing. Figure 2.8 depicts a schematic of the experimental setup. Briefly, a collision atomizer generates particles from jojoba oil. The resulting aerosol flows into a mixing chamber. The replica, located inside the chamber, inhales the aerosol. A sinusoidal flow pattern is generated by an in-house computer controlled pulmonary waveform generator (breathing machine), and an electrical low pressure impactor (ELPI) measures the average number concentration of the aerosol streams.

Regarding particle concentration in the mixing chamber, two significant concepts should be considered: uniformity and equilibrium. In the state of uniformity, the concentration and distribution of the particles does not change from point to point inside the chamber, whereas in the state of equilibrium concentration and distribution of the particles in a particular point remain unchanged through time.

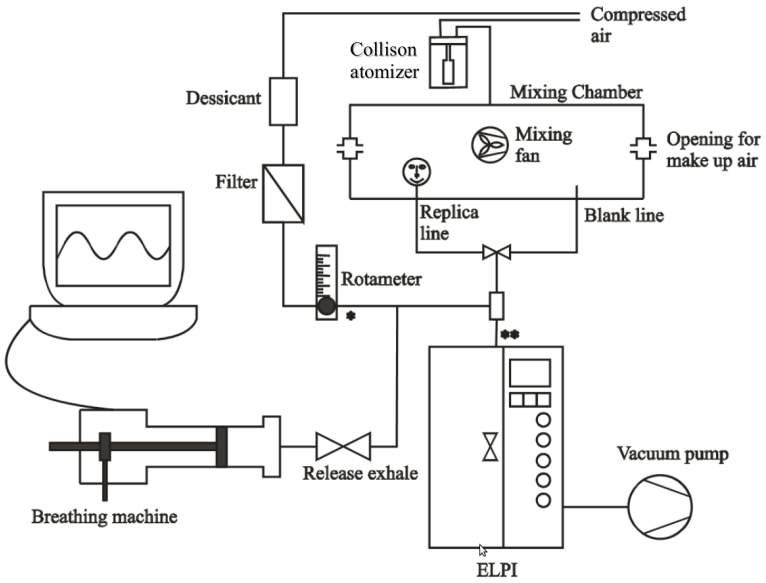

Figure 2.8: Schematic diagram of the experimental setup.

Our mixing chamber is designed in a way to have a uniform distribution of the particles in the chamber volume as soon as the aerosol stream enters the chamber (see Golshahi et al. (2011) for technical details on the mixing chamber). Of crucial importance is the equality of the concentration between the blank line and the nostrils, which is checked before conducting deposition measurements.

Furthermore, to achieve consistent measurements, aerosol samples should be taken from the mixing box when a state of equilibrium is reached. In order to achieve this, prior to measuring the aerosol concentration through the blank and replica lines, the concentration of the different particle sizes at the sampling points is monitored, which asymptotically approach a theoretical equilibrium value. In our experimental conditions (i.e. exposure box size and the tested flow rates) up to 45 min was required to reach equilibrium.

The basic idea for implementing tidal breathing patterns is as follows. Flow rates at points (*) and (**) are adjusted to be equal. During the inhalation phase

of the breathing machine, the flow which is drawn by the breathing machine is simultaneously compensated by the replica line (or alternatively blank line). As a result, the flow pattern generated by the breathing machine is indirectly induced to the replica. During its exhalation phase, the breathing machine does not cause flow in the system, because its exhalation flow rate is released by a valve. The inspiration:expiration duty cycle I:E was 0.5 as in Storey-Bishoff et al. (2008). Flow rates in the lines were measured using a mass flow meter (4143 series, TSI, Shoreview, MN).

In order to determine deposition in the idealized replica, average number concentration of the aerosol streams from the blank line and replica line were measured at discrete particle size ranges using the ELPI, and then subtracted from each other. For more details on the experimental setup see Storey-Bishoff et al. (2008); Golshahi et al. (2011).

2.3 Results and discussion

The results of deposition measurements in the idealized geometry as well as particle sizes and breathing patterns are summarized in Table 2.2.

In Table 2.2, Q is the average flow rate during the inhalation period only, which here is the same as the average flow rate since we use equal inhalation and exhalation times in order to be consistent with Storey-Bishoff et al. (2008).

Deposition data for the idealized geometry as well as from Storey-Bishoff et al. (2008) are depicted vs. impaction parameter, $d_a^2\,Q$, in Fig. 2.9. As reported by Storey-Bishoff et al. (2008), a great deal of inter-subject variability is evident, mainly

d_a (μm)	V_t (L)	bpm	Q (L/min)	$\eta_{deposition}$ (%)
0.79	0.069	44.78	6.18	2.05 ± 0.34
1.28	0.069	44.78	6.18	2.61 ± 0.21
2.03	0.069	44.78	6.18	5.93 ± 0.13
3.20	0.069	44.78	6.18	14.27 ± 0.25
5.32	0.069	44.78	6.18	23.20 ± 2.75
0.79	0.102	30.03	6.13	1.15 ± 0.40
1.28	0.102	30.03	6.13	1.94 ± 0.39
2.03	0.102	30.03	6.13	5.79 ± 1.09
3.20	0.102	30.03	6.13	14.99 ± 2.38
5.32	0.102	30.03	6.13	23.0 ± 10.58
0.79	0.112	44.34	9.93	5.60 ± 0.37
1.28	0.112	44.34	9.93	10.97 ± 0.36
2.03	0.112	44.34	9.93	23.16 ± 0.42
3.20	0.112	44.34	9.93	39.81 ± 0.58
5.32	0.112	44.34	9.93	56.85 ± 2.70
0.79	0.087	58.00	10.09	8.30 ± 0.34
1.28	0.087	58.00	10.09	14.82 ± 0.38
2.03	0.087	58.00	10.09	28.88 ± 0.48
3.20	0.087	58.00	10.09	46.11 ± 0.74
5.32	0.087	58.00	10.09	63.62 ± 4.81
0.79	0.185	29.53	10.93	4.31 ± 0.39
1.28	0.185	29.53	10.93	11.13 ± 0.29
2.03	0.185	29.53	10.93	25.47 ± 0.91
3.20	0.185	29.53	10.93	42.06 ± 1.65
5.32	0.185	29.53	10.93	51.98 ± 11.60

Table 2.2: Results of deposition measurements in the idealized replica, given as mean ± standard deviation (n=5). Here, d_a denotes aerodynamic diameter, V_t denotes tidal volume, bpm is the abbreviation of "breaths per minute, and Q is inhalation flow rate (Q = 2 bpm V_t).

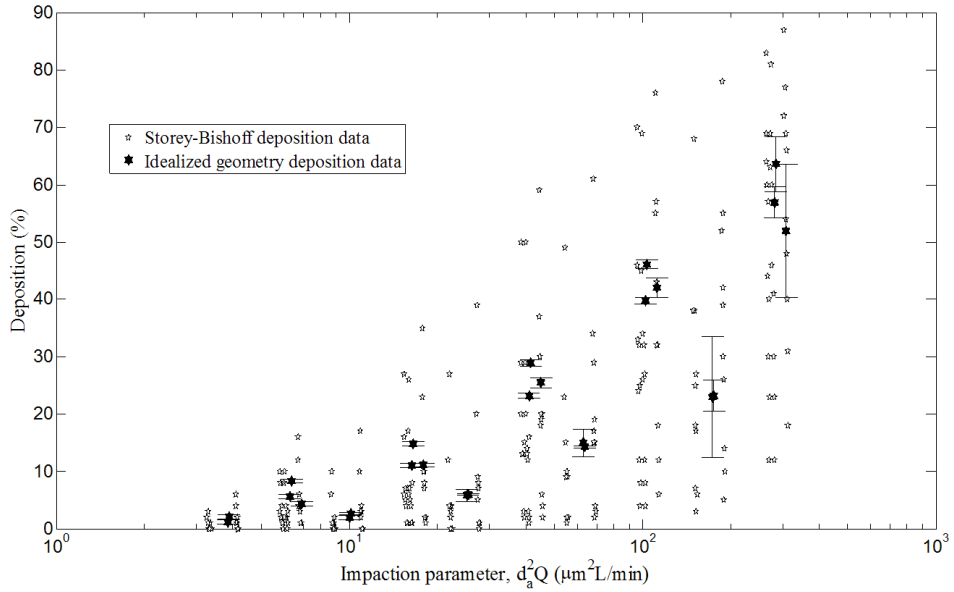

Figure 2.9: Comparison of deposition data for idealized infant nasal airway with those measured by Storey-Bishoff et al. (2008) for 10 in vitro subjects. Error bars for the idealized replica data points indicate standard deviation.

because of inter-subject geometrical differences. Furthermore, even for the idealized geometry, deposition is not captured by a single curve. This form of impaction parameter is used in Fig. 2.9 for two reasons. First, it incorporates the two important parameters which affect impaction: particle size and flow rate. Second, previous in vitro measurements often present data using this widely accepted parameter, so that one can compare deposition data for the idealized nasal airway without further data reduction.

Figure 2.9 indicates that deposition in the idealized geometry lies near the average of the 10 Storey-Bishoff et al. (2008) subjects. This suggests that in spite of its simplified form, the present idealized geometry satisfactorily mimics total extrathoracic deposition in real in vitro airways for particles in the micrometer size range considered here.

As noted earlier, airway geometry is not taken into consideration in the impaction factor $d_a^2\,Q$. This partly accounts for the scattering of deposition data in Fig. 2.9. Instead, a combination of Reynolds and Stokes numbers along with the dimensionless length scale, in the form of $Re^{\alpha}Stk^{\beta}\,(D_h/D_{h_{ave}})^{\nu}$, is a more relevant parameter. For the sake of consistency, the curve fit developed by Storey-Bishoff et al. (2008) to capture the deposition data of the 10 in vitro subjects is adopted here. The curve is trivially modified according to the aforementioned factor of 4 in the length scale, and is written in the following form:

$$\eta = 1 - \left(\frac{566}{566 \;+\; Re^{1.118}\; Stk^{1.057}\; (D_h/D_{h_{ave}})^{-2.84}} \right)^{0.851} \tag{2.1}$$

where D_h and $D_{h_{ave}}$ are the hydraulic diameter of the idealized model (i.e. $4V/A_s$) and the average hydraulic diameter of the 10 real airways, respectively. In the case of the idealized model D_h and $D_{h_{ave}}$ are set to be the same. Also, $Re = 4\,\rho_{air}\,Q\,/\,\pi\,\mu\,D_h$ and $Stk = 2\,\rho_{water}\,d_a^2\,C_c\,Q\,/\,9\pi\,\mu\,D_h^3$. This curve along with the deposition data of the idealized replica and 10 in vitro subjects is shown in Fig. 2.10.

In accord with Fig. 2.9, Fig. 2.10 suggests a satisfactory agreement between deposition in the idealized version and the average of deposition in 10 in vitro subjects. For intermediate values of the impaction parameter in Fig. 2.10, the idealized geometry has somewhat higher deposition than the average of the realistic replicas. This may be due to complexities in the flow that are not captured by the idealized replica. Similar differences at intermediate impaction parameter values are seen in an idealized adult replica (Grgic et al., 2004a) and in an idealized child replica (Golshahi and Finlay, 2012). Although such differences are an anticipated aspect of using a simplified geometry, they have negligible effect when comparing to

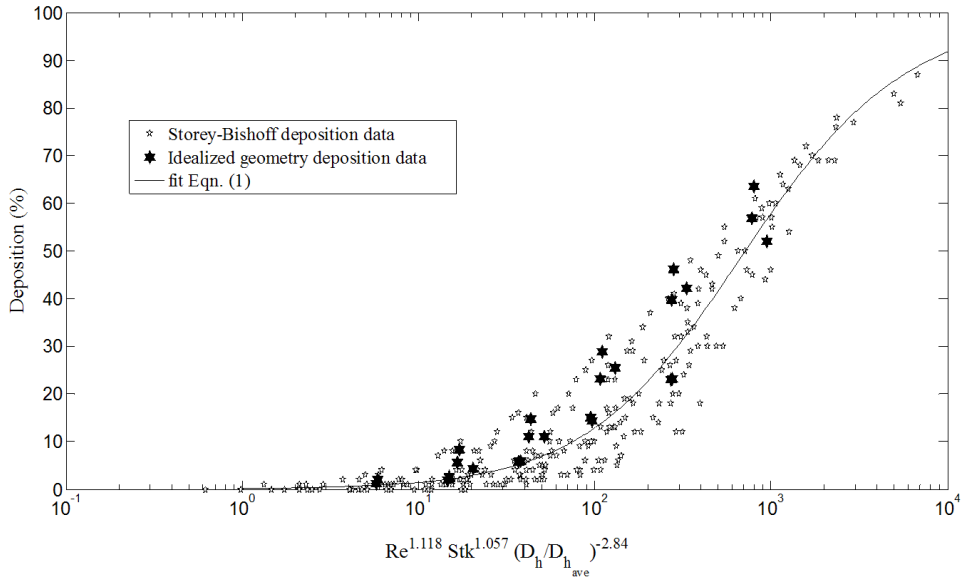

Figure 2.10: Comparison of deposition data for the idealized infant nasal airway with those measured by Storey-Bishoff et al. (2008) for 10 in vitro subjects, plotted using a dimensionless x-axis based on Eq. 2.1.

in vivo data with inhalers in adults (Zhang et al., 2007). Whether the same is true for infants is a topic for future research, although Fig. 2.9 suggests that the present idealized infant geometry should match average infant deposition fairly well.

It may be convenient to have an empirical equation that explicitly fits the deposition data for the present idealized infant geometry. To allow the best collapse of both particle size and flow rate dependence, we follow the form of Eq. 2.1 used by Storey-Bishoff et al. (2008) and fit the following curve to our idealized infant data by minimizing the root mean square of the errors with the aid of MATLABs genetic algorithm toolbox:

$$\eta = 1 - \left(\frac{8.35 \times 10^7}{8.35 \times 10^7 \ + \ Re^{2.812} \ Stk^{1.094}} \right)^{0.4} \tag{2.2}$$

Here D_h=4.8 mm is the hydraulic diameter of our idealized infant geometry,

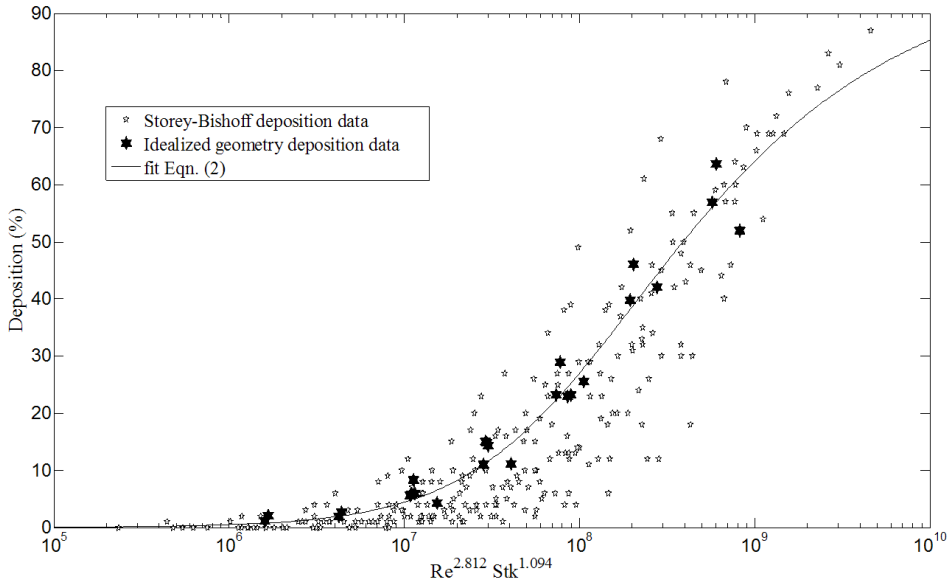

Figure 2.11: Same as Fig. 2.10 but showing curve fit to deposition data of the idealized replica, plotted using a dimensionless x-axis based on Eq. 2.2.

which is the same as the average hydraulic diameter of the replicas studied by Storey-Bishoff et al. (2008). Equation 2.2 along with the deposition data of the idealized replica and 10 in vitro subjects is shown in Fig. 2.11. It is to be noted, however, that for an actual nasal replica, with a hydraulic diameter different from that of the idealized replica, Eq. 2.1 is preferable.

It should be noted that deposition of smaller diameter particles than considered here is affected by diffusion, while that of much larger particles is affected by sedimentation. The present idealized geometry was not developed with either of these deposition mechanisms in mind. For this reason, while Golshahi et al. (2010) examined deposition of ultrafine particles in the same replicas used by Storey-Bishoff et al. (2008), we have not explored the ability of the present idealized geometry to mimic ultrafine aerosol particle deposition.

3. Deposition modeling of hygroscopic saline aerosols in the human respiratory tract: Comparison between air and helium-oxygen as carrier gases

3.1 Introduction

When hygroscopic aerosols are inspired, the size and temperature of the dispersed droplets, as well as the temperature and moisture content of the carrier gas may change due to heat and mass transfer between the dispersed phase and the gas, and also between the gas and the airway walls. This two-way coupled problem is numerically analyzed in this Chapter, with the focus on the effect of using helium-oxygen instead of air as the carrier gas on hygroscopic size changes and deposition of aqueous solution aerosols (Javaheri et al., 2013b). Coefficients of heat and mass transfer in each generation of an idealized respiratory tract are specified based on realistic assumptions. Aerosols of initially isotonic droplets are considered. Differential equations of heat and mass transfer for both the continuous and dispersed phases are numerically solved to simulate the evaporation and condensation. Once the droplet sizes are determined in each respiratory tract generation, deposition is

estimated based on existing correlations for stable particles. The results include regional deposition, in percentage of inhaled NaCl, for both helium-oxygen and air for a variety of size distributions: MMD between 2.5 and 8.5 micrometers and GSD of 1.7. Moreover, the size and temperature variations of the droplets as well as the temperature and humidity variations of the carrier gas are reported. To investigate the impact on deposition caused by hygroscopic size changes, the hygroscopic effectiveness is defined, which specifies the differences in He–O_2 and air deposition caused by hygroscopic size changes. The results, in general, suggest that the lowest deposition fraction in the extra-thoracic region and the highest deposition fraction in the alveolar region correspond to droplets with low mass fraction, inspired with helium-oxygen.

3.2 Methodology

3.2.1 Thermodynamic and transport properties

Helium-oxygen is a low density inhalable gas (nearly 3 times lighter than air, for an oxygen mole fraction of 20%). Its specific heat and transport properties, i.e. kinematic viscosity, thermal conductivity and coefficient of diffusion of water vapor, are remarkably higher than air. The thermodynamic and transport properties of air and helium-oxygen are compared in Table 3.1 for an 80:20 volume mixture of helium:oxygen, which we refer to simply as helium-oxygen or He-O_2 throughout this Chapter. The property values of Table 3.1 are estimated using formula provided by Katz et al. (2011). For a thorough discussion on estimating transport properties see Reid et al. (1987).

Thermodynamic and transport property	Air	Helium-Oxygen
Molecular weight (M) $[\frac{\text{kg}}{\text{k mol}}]$	29	9.6
Density (ρ) $[\frac{\text{kg}}{\text{m}^3}]$	1.139	0.377
Mean free path (λ) [nm]	72	147
Specific heat capacity at constant pressure (c_p) $[\frac{\text{J}}{\text{kg K}}]$	1010	2345
Dynamic viscosity (μ) $[\frac{\text{kg}}{\text{m sec}}]$	1.85×10^{-5}	2.25×10^{-5}
Kinematic viscosity (ν) $[\frac{\text{m}^2}{\text{sec}}]$	1.62×10^{-5}	5.97×10^{-5}
Thermal conductivity (κ) $[\frac{\text{W}}{\text{m K}}]$	0.026	0.114
Thermal diffusivity (α) $[\frac{\text{m}^2}{\text{sec}}]$	2.26×10^{-5}	1.29×10^{-4}
Prandtl number ($Pr = \frac{\nu}{\alpha}$)	0.717	0.463
Coefficient of diffusion of water vapor (Γ) $[\frac{\text{m}^2}{\text{sec}}]$	2.72×10^{-5}	6.26×10^{-5}
Schmidt number ($Sc = \frac{\nu}{\Gamma}$)	0.595	0.954

Table 3.1: Thermodynamic and transport properties of air and helium-oxygen (20 volume percent of Oxygen and 80 volume percent of Helium) at 310 K and 1 atm

The properties of the carrier gas change due to variations of temperature and moisture content, e.g., between 20°C and 37°C, the density and dynamic viscosity of air and He-O_2 vary up to 6%. However, uncertainties involved in calculating the variations of properties of a gas mixture with temperature and humidity are deemed to be comparable with the error of neglecting these variations. Thus, thermodynamic and transport properties of the gases are assumed to remain unaffected by temperature and moisture content.

3.2.2 Aerosol characteristics, breathing pattern, and lung model

Inspired aerosol is assumed to contain initially isotonic droplets with a lognormal size distribution. To deal with heat and mass transfer processes, the continuous droplet size distribution is discretized into N=100 evenly spaced size bins of width 0.2 μm in the range between 0 and 20 μm. The carrier gas is assumed to be initially at 20°C and 99.5% relative humidity (RH). This represents a thermodynamic equilibrium between the gas and a flat surface of an isotonic solution.

The nebulization of pharmaceutical aqueous formulations commonly involves the inhalation of hygroscopic aerosols. Therefore, tidal breathing, which is the normal breathing pattern used with nebulizers, is considered here. Inhalation volume flow rate and tidal volume are assumed to be 18 l/min and 750 cm^3, respectively, which are approximate average values for adult males (Finlay, 2001). Inhalation, hold, and exhalation times are assumed to be 2.5, 0.37, and 2.87 s, respectively; the relative durations are consistent with those suggested by the Task Group on Lung Dynamics (Morrow et al., 1966).

The mass fraction of the dispersed droplets, i.e., the total mass of droplets per unit volume of the carrier gas, is an important parameter in the study of hygroscopic effects. Given that the droplets are initially isotonic, for a particular breathing pattern, the mass fraction of droplets could also be specified in terms of total inhaled salt (NaCl) per minute, denoted by ψ. The effect of droplet mass fraction on hygroscopic size changes will be examined here by considering three values of ψ: 0.01 mg/min, corresponding to low droplet mass fraction; 0.1 mg/min, corresponding to medium droplet mass fraction; and 1.0 mg/min, corresponding to high droplet

mass fraction. The typical range of nebulizer outputs is between 0.1–1.0 g/min, depending on the nebulizer type. This corresponds to a range of ψ between 0.39–3.9 mg/min. In terms of nebulizer output, ψ=1.0 mg/min corresponds to a nebulizer aerosol output of 0.255 g/min, ψ=0.1 mg/min corresponds to a nebulizer aerosol output of 0.0255 g/min, and ψ=0.01 mg/min corresponds to a nebulizer aerosol output of 0.00255 g/min. This indicates that the high value of ψ lies in the typical range of nebulizer outputs, while the medium and low values of ψ are chosen to represent the cases where hygroscopic effects are more noticeable.

A cylindrical tube with 1.87 cm diameter and 4.0 cm length represents the mouthpiece. Its wall is assumed to be adiabatic and impermeable, i.e., no heat and mass transfer takes place at the wall. The Alberta Idealized Mouth Throat (Stapleton et al., 2000) is adopted as the upper airway geometry for determining heat and mass transfer coefficients and for determining particle residence times. The symmetric lung model of Finlay et al. (2000), with the lung volume (functional residual capacity) scaled to 3000 cm^3, is used for the thoracic airways geometry.

3.2.3 Heat and mass transfer from airway walls

When hygroscopic aerosol is inhaled, heat and mass transfer occur by two mechanisms: 1) convective transfer between the carrier gas and walls of the airway, and 2) diffusive transfer between the individual droplets and the carrier gas. Convective heat and mass transfer coefficients can be calculated based on estimates of temperature and humidity profiles in the respiratory tract when no droplets are present in the inhaled gas (Finlay and Stapleton, 1995). In order to estimate the temperature and humidity of the gas flow for air, Ferron et al. (1988-a) solved the governing

transport equations in cylindrical geometries with laminar parabolic velocity profiles. They considered the effect of turbulence in the upper airways via additional eddy diffusivity. Daviskas et al. (1990) used the analytical solution of a one dimensional transient diffusion equation to estimate temperature and humidity. To obtain more realistic results, they also modified the diffusivity coefficient based on the volume flow rate. Unfortunately, the previous estimations of temperature and humidity in the respiratory tract are for air, not He-O_2. Moreover, the available profiles are obtained from highly simplified mathematical models. In the present study, we instead calculate heat and mass transfer coefficients in the extra-thoracic airways using computational fluid dynamics (CFD) simulations of heat and mass transport in the Alberta Idealized Mouth Throat (Stapleton et al., 2000). Fluid flow as well as heat and water vapor transfer is simulated in this mouth-throat geometry using Ansys CFX (Release 12.1) with Dirichlet boundary conditions at the walls for temperature (310 K) and water vapor concentration (99.5% RH). A total number of 1577726 elements (469502 nodes) was used, which is sufficient to yield grid converged results based on previously published works in this geometry (Stapleton et al., 2000; Heenan et al., 2003). Given that the values of the Pr and Sc numbers for air and helium–oxygen mixture are of the order of magnitude of 1.0 (Table 3.1), the thickness of the hydrodynamic, thermal, and mass transfer boundary layers are deemed to be almost similar. Thus, regarding grid convergence, this grid size is thought to be also sufficient for heat and mass transfer simulations. Miyawaki et al. (2012) conducted Large Eddy Simulations for different volume flow rates through a realistic replica of a human mouth-throat, and found that depending on the physical properties of the gas, laminar, transitional, or turbulent flow may occur. They defined a Reynolds number based on the hydraulic diameter of the trachea (Re_t) and

found that the critical Reynolds for transition between laminar and turbulent flows (Re_{t_c}) is approximately 430. In the present study, for the volume flow rate of 18 l/min, airflow in the upper airway was therefore assumed turbulent ($Re_t = 1474$), and a low Reynolds number SST turbulence model was used, while helium-oxygen flow remained laminar ($Re_t = 400$). The average coefficients of heat transfer, $\bar{h}$, and mass transfer, $\bar{g}$, in the mouth, throat, and trachea are obtained in a post processing operation using the following formula:

$$\bar{h} = \frac{\rho_g \, c_{p_g} [\iint^{out} T \, \mathbf{V} \, . \, d\mathbf{S} - \iint^{in} T \, \mathbf{V} \, . \, d\mathbf{S}]}{A_{wall} \, (T_{wall} - T_\infty)} \tag{3.1}$$

$$\bar{g} = \frac{[\iint^{out} C \, \mathbf{V} \, . \, d\mathbf{S} - \iint^{in} C \, \mathbf{V} \, . \, d\mathbf{S}]}{A_{wall} \, (C_{wall} - C_\infty)} \tag{3.2}$$

Here, C is the water vapor concentration, T is temperature, $\mathbf{V}$ is the gas velocity and the subscript ∞ designates the bulk gas. c_{p_g} is the specific heat capacity at constant pressure and ρ_g is the density of the carrier gas, as given in Table 3.1. The above formula are simply derived by considering conservation of energy and mass for a control volume coinciding with the mouth, throat or trachea (Bergman et al., 2011). Calculated values of heat and mass transfer coefficients in the extra-thoracic passages for the volume flow rate of 18 l/min using this approach are summarized in Table 3.2.

For heat and mass transfer coefficients distal to the trachea, the airway passages are assumed to be circular cylinders with diameter D from our idealized lung model (Finlay et al., 2000). For the volume flow rate of 18 l/min, the value of Reynolds number in these passages is always less than 1850; thus we assume laminar flow there. The theory of laminar heat and mass transfer in tubes is well developed.

	Air		$He\text{-}O_2$	
	$\bar{h}$ $[\frac{W}{m^2 K}]$	$\bar{g}$ $[\frac{m}{sec}]$	$\bar{h}$ $[\frac{W}{m^2 K}]$	$\bar{g}$ $[\frac{m}{sec}]$
Mouth	14.9	0.0144	25.3	0.0189
Throat	27.0	0.0259	42.4	0.0311
Trachea	31.5	0.0309	53.71	0.0375

Table 3.2: Convective heat and mass transfer coefficients in the upper airways for volume flow rate of 18 l/min, for both air and helium-oxygen

However, the effect of hydrodynamic and thermal development should be considered. An accurate numerical solution for simultaneously developing laminar flow in an isothermal circular tube has been presented by Jensen (1989). The results of this simulation involve the average Nusselt number ($Nu_{ave} = \bar{h}D/\kappa$) as a function of dimensionless tube length and the Prandtl number ($Pr = \nu/\alpha$). Considering the similarity between mass and heat transfer, the average Sherwood number ($Sh_{ave} = \bar{g}D/\Gamma$) as a function of dimensionless tube length, and Schmidt number ($Sc = \nu/\Gamma$), can be also inferred from Jensen's data. The average values of the coefficients of heat and mass transfer in the thoracic airways are directly calculated using Nu_{ave} and Sh_{ave}.

In each generation, the heat and mass transfer rate from airway walls to the aerosol bolus can be written as

$$\dot{q}_{wall} = \bar{h}\,\tilde{A}\,(T_{wall} - T_{\infty}) \tag{3.3}$$

$$\dot{m}_{wall} = \bar{g}\,\tilde{A}\,(C_{wall} - C_{\infty}) \tag{3.4}$$

where $\tilde{A}$ is the area of interface between the bolus and the airway walls, and is

estimated as follows:

$$\tilde{A} = \tilde{V}\,\frac{A}{V} \tag{3.5}$$

Here, $\tilde{V}$ is the volume of the bolus and A and V are the internal area and volume of the airway, respectively.

3.2.4 Heat and mass transfer between continuous and dispersed phases

Hygroscopic size changes amount to a transfer of mass (water vapor) between the carrier gas and the dispersed droplets normally associated with heat transfer, yielding differential equations of heat and mass transfer that govern the diameter d_i and temperature T_i of the droplets in the ith size bin. These equations are discussed in detail by Fuchs (1959), Mason (2010), and Finlay (2001), and are given here for the sake of completeness and clarity.

The equation governing the diameter d_i of the ith droplet size can be written as:

$$\frac{\mathrm{d}d_i}{\mathrm{d}t} = \frac{-4\,\Gamma\,(C_i - C_\infty)}{\rho_w\,d_i} \tag{3.6}$$

where C_i is the water vapor concentration at the surface of the ith droplet size. For solution droplets, the water vapor concentration at the surface is less than that for droplets of pure water. In contrast, the surface curvature tends to increase the vapor concentration at the surface (via the Kelvin effect). For the present saline droplets, these effects are formulated using the correlations given by Cinkotai (1971).

An equation of heat transfer governs the temperature of the ith droplet size:

$$\rho\, c_p\, \frac{{d_i}^2}{12}\, \frac{\mathrm{d}T_i}{\mathrm{d}t} = -L\, \Gamma\, (C_i - C_\infty) - \kappa\, (T_i - T_\infty) \tag{3.7}$$

Here, c_p is the specific heat capacity and ρ is the density of the saline droplet, and L is the latent heat of evaporation of the liquid water, which is assumed to be independent of temperature.

3.2.5 Variation of temperature and vapor concentration of the carrier gas

In the two way coupled mathematical model for heat and mass transfer, temperature and moisture content of the carrier gas change due to transport of heat and vapor with dispersed droplets and airway walls, and are governed by:

$$\rho_g\, c_{p_g}\, \tilde{V}\, \frac{\mathrm{d}T_\infty}{\mathrm{d}t} = \dot{q}_{wall} + \sum_{i=1}^{N} n_i\, \tilde{V}\, \dot{q}_{c_i} \tag{3.8}$$

$$\tilde{V}\, \frac{\mathrm{d}C_\infty}{\mathrm{d}t} = \dot{m}_{wall} - \sum_{i=1}^{N} n_i\, \tilde{V}\, \frac{\mathrm{d}m_i}{\mathrm{d}t} \tag{3.9}$$

Here, n_i is the number of droplets in the ith size bin per unit volume and dm_i/dt is the rate of change of mass of the ith size which could be simply derived from Eq. 3.6. $\dot{q}_{c_i}$ is the rate of conductive heat transfer from the surface of the ith droplet size:

$$\dot{q}_{c_i} = 2\, \pi\, d_i\, \kappa\, (T_i - T_\infty) \tag{3.10}$$

Substituting from Eq. 3.3, 3.4, 3.6, and 3.10 into Eq. 3.8 and 3.9 yields:

$$\rho_g \, c_{p_g} \, \frac{\mathrm{d}T_\infty}{\mathrm{d}t} = \frac{\bar{h} \, A}{V}(T_{wall} - T_\infty) + \sum_{i=1}^{N} 2 \, \pi \, \kappa \, n_i \, d_i \, (T_i - T_\infty) \tag{3.11}$$

$$\frac{\mathrm{d}C_\infty}{\mathrm{d}t} = \frac{\bar{g} \, A}{V}(C_{wall} - C_\infty) + \sum_{i=1}^{N} 2 \, \pi \, \Gamma \, n_i \, d_i \, (C_i - C_\infty) \tag{3.12}$$

Equations 3.6, 3.7, 3.11, and 3.12 represent a set of moderately stiff 2N+2 non-linear, coupled, ordinary differential equations governing 2N+2 unknown functions of time, associated with the diameters and temperatures of the N droplet sizes and bulk temperature and water vapor concentration of the carrier gas. Finlay and Stapleton (1995) and Stapleton et al. (1994) validated this mathematical model for both small and large number of droplets per unit volume, while Saleh and Shihadeh (2007) provided experimental validation.

Because of the stiffness of the equations, the CVODE (*the C Version of a Variable Coefficient ODE Solver*) routine of the Lawrence Livermore National Laboratory, Numerical Mathematics Group (Cohen and Hindmarsh, 1994) was used. The underlying integration method implemented in CVODE is a variable order Backward Differentiation Formula (BDF), an implicit scheme with satisfactory stability for stiff ODEs. To validate the numerical analysis, the ODE system was also solved with the aid of an in- house developed code, using the explicit Runge-Kutta-Fehlberg (RKF45) algorithm, with adaptive variable size time step. A validation run was performed for air, initially at 20°C and 50% RH, carrying a medium mass fraction (ψ=0.1 mg/min) of polydisperse droplets with MMD of 6 μm and GSD of 1.7. Maximum differences between the predictions of CVODE and RKF45 were observed during the first few hundred time steps of CVODE, when droplets and air were far

from equilibrium. However, even for that case, the results including the size and temperature of the droplets as well as the temperature and RH of the air, were always less than 3% different. Due to excessively small time steps, the execution time for the RKF45 was considerably higher compared to the implicit BDF.

3.2.6 Deposition calculation

To determine deposition, the tidal volume is considered to comprise several hundred hypothetical small segments, with each segment reaching different depths in the lung. As a result, only a fraction of the tidal volume passes entirely through each lung generation. The amount of drug delivered to each generation by each hypothetical segment of the gas depends on its final destination in the lung. In order to accommodate this effect, the tidal volume is discretized into 500 small segments. Each segment is a small aerosol bolus which is tracked during inhalation, inspiratory pause and exhalation. Once the droplet sizes are calculated in each lung generation, deposition is estimated based on previously published equations for stable particles.

In the thoracic airways, the following equations are used to estimate the deposition: Chan and Lippmann (1980) for inertial impaction, Heyder (1975) and Heyder and Gebhart (1977) for sedimentation, and Ingham (1975) for diffusion. Density of the carrier gas, which is the distinguishing physical property of the helium-oxygen, does not appear in these equations. Dynamic viscosity, however, which always tends to decrease the deposition, and is 22% higher for helium-oxygen than for air, appears in all of these equations. See Finlay (2001) for a comprehensive discussion of these equations.

In the extra-thoracic airways, deposition of micrometer size droplets is controlled

by impaction. Dimensional analysis reveals that the Reynolds and Stokes numbers determine impaction. Therefore, when deposition data are reported *vs.* a combination of Re and Stk, they are believed to be applicable for all carrier gases. Sandeau et al. (2010) numerically simulated the deposition in a reconstructed oral extra-thoracic replica for air and helium- oxygen. Using $Stk\,Re^{0.3}$ as the impaction parameter, their deposition data for the two gases successfully collapsed into a single curve. To confirm this notion, in a supplementary part of the present study, deposition of nebulized stable jojoba oil droplets, inhaled with helium-oxygen was experimentally measured, using the Alberta Idealized Mouth Throat at flow rates from 30-90 l/min. The aerosol stream was monitored using a Next Generation Impactor (NGI), with and without the Alberta Idealized Throat in line. This allowed determination of deposition fraction in the Alberta Idealized Throat for droplets in each size range of the NGI. In Fig. 3.1, the results of these deposition measurements are plotted *vs.* $Stk\,Re^{0.37}$ and compared with the deposition correlation of Grgic et al. (2004b). Satisfactory agreement is observed. This evidence supports the reasonable hypothesis that available deposition correlations of air can be used for other gases provided two conditions are fulfilled. First, deposition is reported *vs.* $Re^{\alpha}\,Stk^{\beta}$, and second, the correlation should be used for its valid ranges of Stk and Re numbers. The second condition means that only correlations which are valid for low Re ranges are applicable for helium-oxygen (since the much lower density of helium-oxygen results in much lower Re than in air).

Recently, Golshahi et al. (2013) have conducted an *in-vitro* study on deposition of micrometer size particles in extra-thoracic airways during tidal oral breathing. This study includes volume flow rates as low as 12.2 l/min, corresponding to the low Re number range, and deposition is reported *vs.* $Stk^{3.03}\,Re^{0.25}$. Moreover, deposition

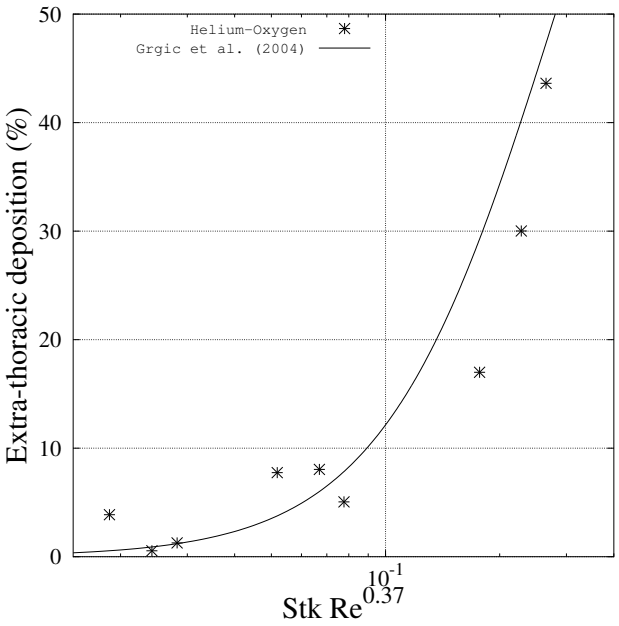

Figure 3.1: Extra-thoracic deposition of stable particles shown as a function of $Stk\,Re^{0.37}$. The solid curve is the correlation of Grgic et al. (2004b) for deposition measurements in air, while the markers indicate the results of deposition measurements in helium-oxygen.

is measured during tidal breathing which is the breathing pattern used in the present study. As a result, the following correlation suggested by Golshahi et al. (2013) is adopted here for estimating extra-thoracic deposition of stable particles, for both air and helium-oxygen:

$$\eta = 1 - \frac{1}{1 + 1.51 \times 10^5 \left(Stk^{3.03}\, Re^{0.25}\right)} \tag{3.13}$$

Carrier gas density appears in Eq. 3.13 via the Reynolds number. Thus, even though deposition in the thoracic airways does not explicitly depend on carrier gas density, its influence on extra-thoracic deposition will indirectly affect thoracic deposition.

3.3 Results and discussion

3.3.1 Carrier gas relative humidity

For low mass fraction (ψ=0.01 mg/min), the carrier gas remains virtually unaffected by the dispersed droplets, and hygroscopic effects are more easily explained. Of practical interest, however, is the high mass fraction (ψ=1.0 mg/min) which is comparable to the mass fraction of actual nebulized aerosols. Therefore, the variations of relative humidity and temperature of the carrier gas as well as the diameter and temperature of the droplets are presented in detail here for both low and high mass fractions. Full presentation of all three mass fractions will be given when examining deposition in a later subsection.

Relative humidity of the carrier gas has a pronounced effect on the shrinkage and growth of the droplets. For air and helium-oxygen, it is given as a function of time of transit through the mouthpiece and respiratory tract in Fig. 3.2, for ψ=0.01 mg/min (left panel) and ψ=1.0 mg/min (right panel). For ψ=0.01 mg/min, relative humidity changes only because of vapor and heat transfer from the airway walls. The former tends to increase the relative humidity, whereas the latter tends to decrease it. Therefore, variation of relative humidity depends on the relative rate of vapor and heat transfer processes. For ψ=1.0 mg/min , relative humidity changes partly because of vapor and heat transfer from the walls, and partly because of heat and vapor exchange with the dispersed droplets.

To investigate the effect of heat and vapor transfer from the walls on the gas, we define a dimensionless number β to be the ratio of thermal diffusivity to the

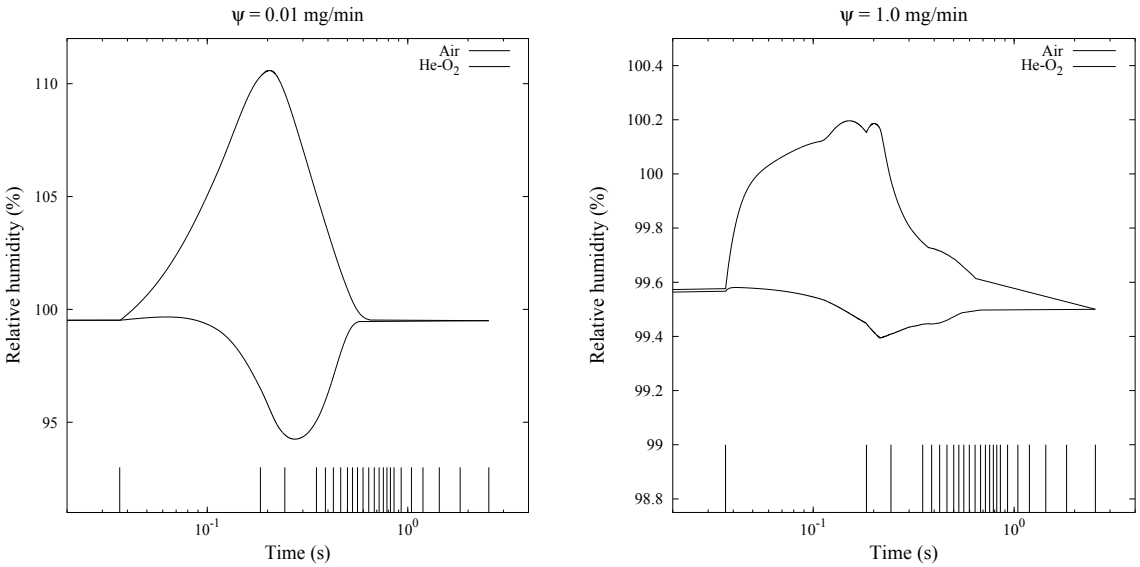

Figure 3.2: Relative humidity of the carrier gas as a function of time for a polydisperse aerosol (MMD=6.0 μm, GSD=1.7) with low mass fraction of droplets, ψ=0.01 mg/min, (left), and high mass fraction of droplets, ψ=1.0 mg/min, (right). The vertical lines at the bottom of the figures determine the generation, e.g., the time interval prior to the first vertical line represents the mouthpiece, the time interval between the first and the second line represents the mouth, followed by the throat, the trachea, the main bronchi, etc.

coefficient of diffusion of water vapor:

$$\beta = \frac{\alpha}{\Gamma} \tag{3.14}$$

A lower value of β implies that transport of water vapor from airway walls is more effective than transport of heat. Considering that vapor transfer tends to increase the RH and heat transfer tends to decrease that, a lower value of β will result in a higher relative humidity. The value of β is 2.06 for helium-oxygen and 0.83 for air. This suggests that in similar conditions, compared with helium-oxygen, higher relative humidity for air should be expected, as is confirmed in Fig. 3.2.

Isotonic droplets, on the other hand, tend to prevent the deviation of RH from 99.5%, which is the value of RH at the flat surface of an isotonic solution. This effect

is also evident in Fig. 3.2: For ψ=0.01 mg/min, deviation of RH from 99.5% is much more than that for ψ=1.0 mg/min, in which the number of droplets is sufficient to influence their carrier gas.

3.3.2 Variation of droplet size

The rate of evaporation of droplets, as is defined in Eq. 3.6, depends on the aerosol size distribution. For a monodisperse or narrow size distribution, the droplets evaporate at essentially the same rate. For a wide size distribution, in contrast, small droplets evaporate much faster than the large ones, since the characteristic time of evaporation is proportional to the inverse square of droplet diameter (see Eq. 3.6).

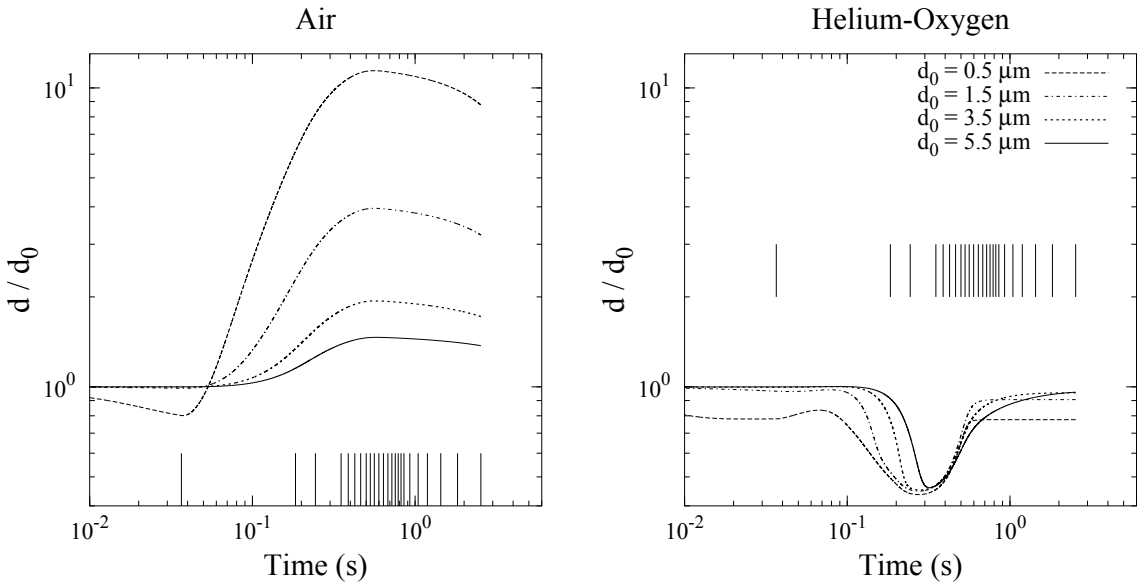

Figure 3.3: Variation of droplet diameters in an inspired polydisperse aerosol (MMD=6.0 μm, GSD=1.7) with low mass fraction of droplets (ψ=0.01 mg/min). See Fig. 3.2 for explanation of the vertical lines in the figures.

The variation of the diameter of the droplets, normalized by the initial diameter, as a function of time of transit through the mouthpiece and respiratory tract, is

given in Fig. 3.3 for ψ=0.01 mg/min and in Fig. 3.4 for ψ=1.0 mg/min. These figures compare the role of air and helium-oxygen as the carrier gases in growth and shrinkage of different droplet sizes in a polydisperse aerosol (MMD=6 μm, GSD=1.7). Figures 3.3 and 3.4 confirm that smaller droplets are more sensitive and respond faster to the variations in the thermodynamic state of the carrier gas. The behavior of droplets initially larger than 5.5 μm can also be predicted by considering the trends of Fig. 3.3 and 3.4. They follow the pattern of the size change of $d_0 = 5.5$ μm droplets, but always with a smaller rate of variation.

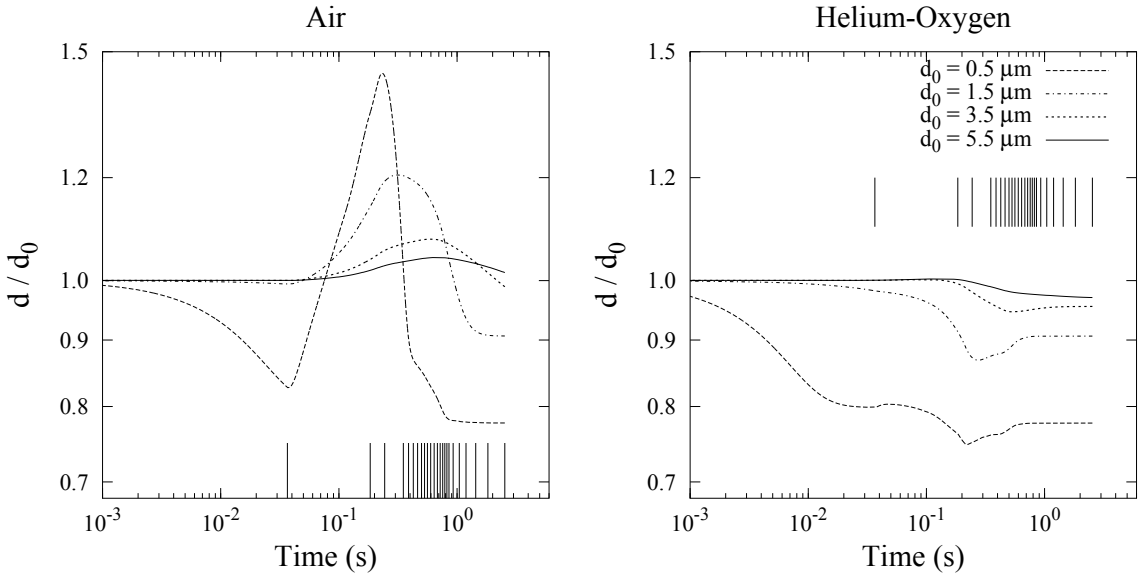

Figure 3.4: Variation of droplet diameters in an inspired polydisperse aerosol (MMD=6.0 μm, GSD=1.7) with high mass fraction of droplets (ψ=1.0 mg/min). See Fig. 3.2 for explanation of the vertical lines in the figures.

There is a close relationship between the relative humidity of the carrier gas and the shrinkage and growth of the droplets. Droplets can grow larger than their initial size only when the vapor pressure in their surrounding gas is more than vapor pressure at their surface vicinity. The growth of droplets inspired with air (Fig. 3.3 and 3.4, left panel) is because of the supersaturation of air (see Fig. 3.2), while the

shrinkage of those droplets is because of their curvature (Kelvin effect). For droplets inspired with helium-oxygen (Fig. 3.3 and 3.4, right panel), however, both curvature and undersaturation of He-O_2 give rise to evaporation.

The final thermodynamic state of the inspired aerosol is determined by the liquid covering the airway walls, which is an isotonic saline solution. In other words, the droplets and the carrier gas finally come into thermodynamic equilibrium with this liquid. In this state, the vapor pressure at the surface of the airway walls and at the surface of the dispersed droplets should be equal. The latter is determined by droplet temperature, droplet size (curvature), and ionic composition of the droplet. The rate at which droplets approach their final size depends on the transport properties of the carrier gas, i.e. faster in helium-oxygen and slower in air. Figures 3.3 and 3.4 make it obvious that droplets inhaled with helium-oxygen can reach their final size at the end of the inhalation time, but those inhaled with air may need more time to reach equilibrium with their environment. Given that the inhalation time is much more than the characteristic time of the size change of droplets, and also that the carrier gas reaches its equilibrium state by the end of inhalation and remains in equilibrium, the size change of droplets during exhalation is deemed to be negligible.

Since the amount of drug contained in droplets varies with the cube of droplet diameter, it is the larger particles that significantly determine drug delivery. For higher mass fractions, the faster evaporation of smaller sizes can saturate the surrounding gas, thus restricting the slower evaporation of larger droplets. As a result, the shrinkage of large droplets, containing most of the drug, is insignificant, and differences in hygroscopic effects in helium-oxygen and air trivially impact regional drug delivery.

3.3.3 Carrier gas and droplet temperature

The temperature of the dispersed droplets is obtained from Eq. 3.7. The left hand side of Eq. 3.7, which depends on the droplet diameter, is negligible compared to either of the two terms in the right hand side. As a result, all the droplets, regardless of their size, experience the same temperature during their progress through the airways (Finlay, 2001, chap. 4).

The temperature of air and helium-oxygen, as well as the temperature of the droplets, are given as a function of time of transit through the mouthpiece and the respiratory tract in Fig. 3.5, for ψ=0.01 mg/min (left panel), and for ψ=1.0 mg/min (right panel).

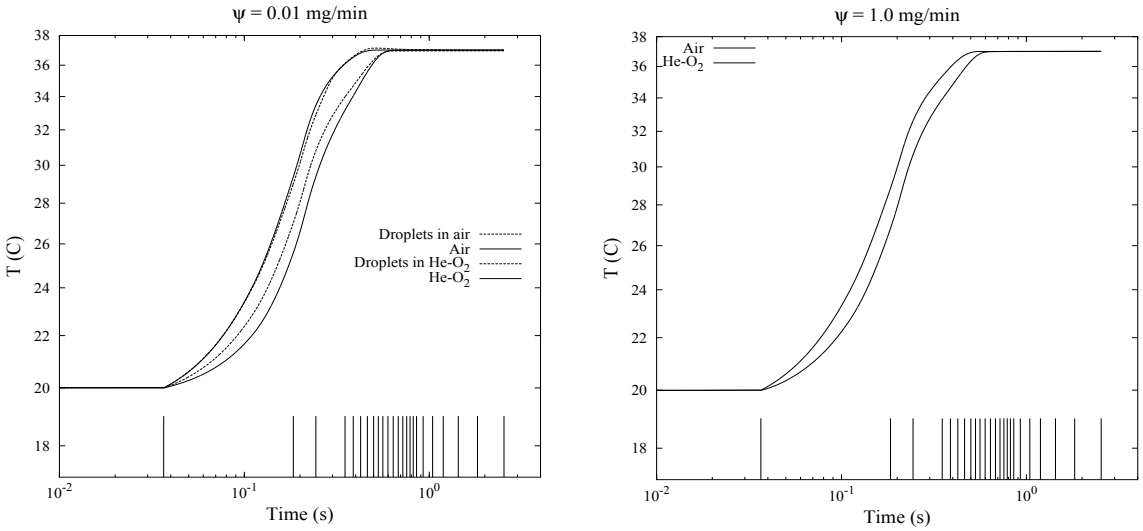

Figure 3.5: Temperature of the carrier gas and different droplet sizes as a function of time in an inspired polydisperse aerosol (MMD=6.0 μm, GSD=1.7) with low mass fraction of droplets, ψ=0.01 mg/min, (left), and high mass fraction of droplets, ψ=1.0 mg/min, (right). See Fig. 3.2 for explanation of the vertical lines at the bottom of the figures.

For low mass fraction of droplets the temperature of the carrier gas remains virtually unaffected by the dispersed droplets and varies due to heat transfer from the airway walls. In this case, a slight temperature difference between droplets and gas

is detectable (Fig. 3.5, left panel). The implication of higher thermal conductivity of helium-oxygen is that the temperature difference between air and droplets is more than the temperature difference between helium-oxygen and droplets.

In terms of heat transfer between the droplets and the gas, an increase in number concentration of droplets has the same effect as an increase in the thermal conductivity of the gas (see Eq. 3.11): This means that for high concentration of droplets, no detectable temperature difference between the gas and the droplets should be expected. In Fig. 3.5, right panel, the curve designated "Air", actually illustrates the temperature of air and its droplets, and similarly for "He-O_2".

3.3.4 Regional deposition *vs.* droplet size

Regional deposition data, for both helium-oxygen and air are given as a function of initial MMD, in the range of 2.5-8.5 μm. This includes fractional deposition for extra-thoracic, tracheo- bronchial, and alveolar regions. Because the salt content of the hygroscopic droplets remains constant, fractional deposition is defined as the regional deposited NaCl divided by total inhaled NaCl. The effect of droplet mass fraction is examined by considering three values of ψ, i.e. the total mass of droplets per unit volume of the carrier gas.

Not all the differences between air deposition and helium-oxygen deposition can be attributed to hygroscopic effects, since differences in deposition of stable particles can occur, for example, due to the differences in Re and Stk in the extra-thoracic deposition (Eq. 3.13). In particular, for equal volume flow rates through a passage, the Reynolds number of the airflow is nearly three times that of helium-oxygen. Therefore, when helium-oxygen is inspired, turbulence may be reduced in the up-

per respiratory tract, and lower deposition due to turbulence mixing is expected (Darquenne and Prisk, 2004; Peterson et al., 2008). For stable aerosols, most of the advantages of helium-oxygen over air are attributed to its low density (Ari and Fink, 2010).

All the differences between the deposition of volatile droplets and their corresponding stable particles are actually attributed to the hygroscopic effects. In order to examine the effect of hygroscopicity on the regional deposition, the variable *hygroscopic effectiveness* is defined as the following

$$\lambda = \Big|deposition\ in\ air - deposition\ in\ He\text{-}O_2\Big|_{Hygroscopic\ droplets} - \Big|deposition\ in\ air - deposition\ in\ He\text{-}O_2\Big|_{Stable\ particles} \tag{3.15}$$

In addition, λ_{low}, λ_{med}, and λ_{high} designate the hygroscopic effectiveness in low, medium, and high mass fractions, respectively. A negative value of λ indicates that hygroscopicity decreases the difference between deposition with helium-oxygen *vs.* air. A value of $\lambda = 0$ means that hygroscopicity does not affect the difference between deposition with helium-oxygen *vs.* air, while a positive value of λ indicates that hygroscopicity increases the difference between deposition with helium-oxygen *vs.* air.

Deposition in extra-thoracic, tracheo-bronchial, and alveolar regions is illustrated in Fig. 3.6, 3.7, and 3.8, respectively. These figures make obvious that for droplets inspired with air, hygroscopicity tends to increase the extra-thoracic and tracheo-bronchial deposition, and decrease the alveolar deposition. In contrast, when droplets are inspired with helium-oxygen, hygroscopicity tends to decrease the

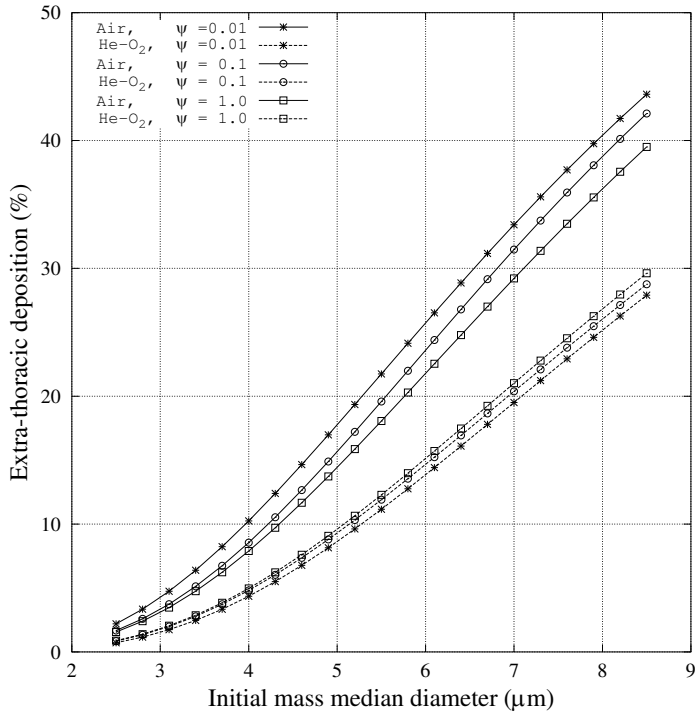

Figure 3.6: Extra-thoracic deposition as a function of initial MMD for inhaled polydisperse aerosols with GSD=1.7.

extra-thoracic and tracheo-bronchial deposition, and increase the alveolar deposition. This is in accord with the implications of Fig. 3.2–3.4. It could be argued that when droplets are inhaled with air, because of the low value of β, supersaturation occurs; thus droplets undergo condensational growth; thereby increasing deposition in the upper airways. On the other hand, when droplets are inhaled with helium-oxygen, due to the high value of β, gas always remains undersaturated; thus droplets evaporate and shrink; thereby increasing their penetration into the alveolar region. This explains how the properties of the gas can change the deposition pattern via hygroscopic size changes.

Helium-oxygen is suitable for drug delivery to patients with severely obstructed lungs. Modeling of diseased airways, however, is beyond the scope of the present

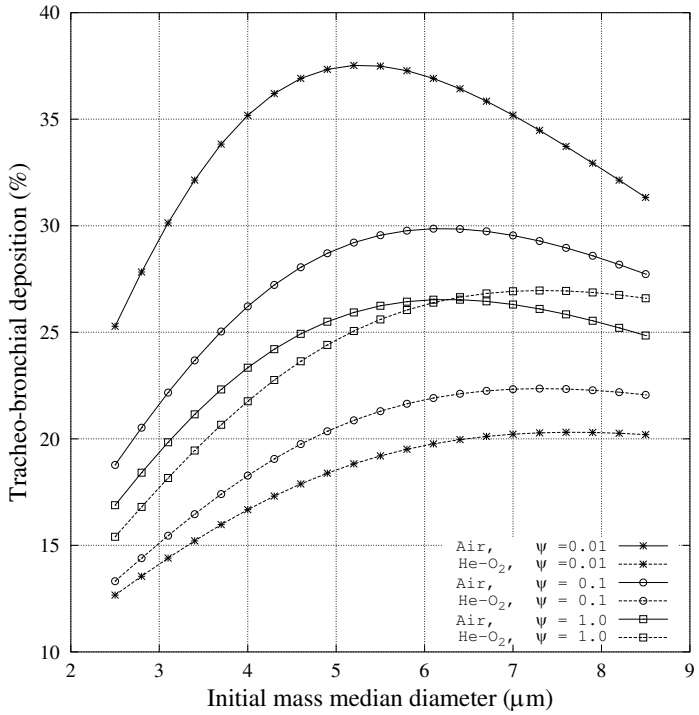

Figure 3.7: Tracheo-bronchial deposition as a function of initial MMD for inhaled polydisperse aerosols with GSD=1.7.

manuscript. Nevertheless, the trends observed here will carry over to aerosol behavior in diseased lungs. Indeed, the parameter β helps predict some aspects which are independent of the geometry of the airway. That is, due to the combination of vapor and heat transfer from the airway walls, the increase in RH of the air is more than the increase in RH of the helium-oxygen (the RH of the helium-oxygen sometimes even decreases: see e.g. Fig. 3.2). The immediate result of this is that overall, droplets have more chance to evaporate in helium-oxygen, yielding smaller sizes which may be more favorable for drug delivery for both normal and diseased lungs.

The regional values of λ, for MMD of 6 μm and GSD of 1.7, are given in Table 3.3. For the present initial conditions and breathing pattern, λ is always positive,

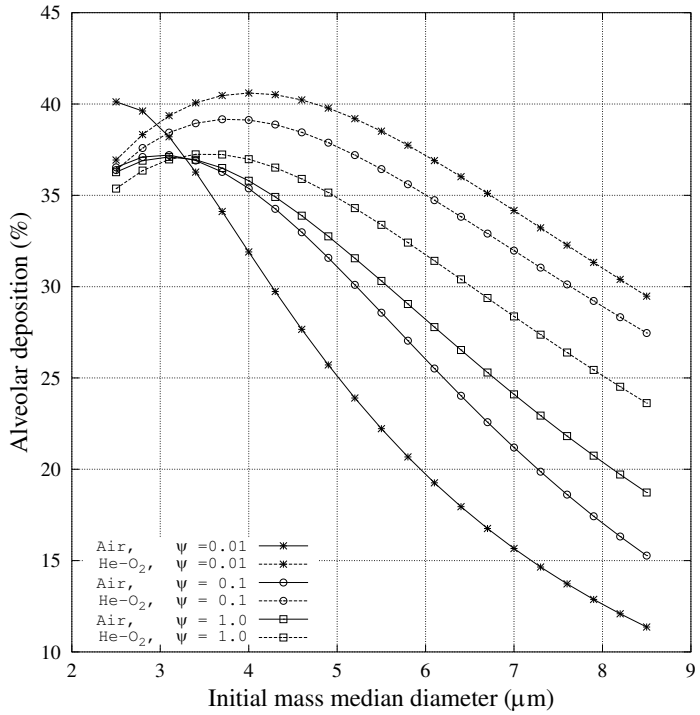

Figure 3.8: Alveolar deposition as a function of initial MMD for inhaled polydisperse aerosols with GSD=1.7.

i.e. hygroscopicity increases the difference between deposition with helium-oxygen *vs.* air. This increase is insignificant for high mass fraction, and noticeable for low mass fraction.

	Extra-thoracic	Tracheo-bronchial	Alveolar
$\lambda_{low}(\%)$	5.6	23.1	14.8
$\lambda_{med}(\%)$	2.7	13.8	6.4
$\lambda_{high}(\%)$	0.4	6.0	0.9

Table 3.3: Regional values of the *hygroscopic effectiveness* (λ) for MMD of 6 μm and GSD of 1.7. See Eq. 3.15 for the definition of λ.

4. Size manipulation of hygroscopic saline droplets: application to respiratory drug delivery

4.1 Introduction

The size distribution of pharmaceutical aerosols delivered by nebulizers normally contains a fraction that is larger than is optimal for drug delivery to the lungs; thus a noticeable fraction of droplets deposits in the extra-thoracic airways. However, because of the volatile nature of these droplets, their size can be reduced by controlled evaporation. Two approaches to size reduction are investigated in this Chapter. They are aimed at altering the vapor pressure balance between the surface of the droplets and the carrier air. In the first approach, the aerosol stream is heated. This increases the vapor pressure at the surface of the droplets, allowing them to evaporate and shrink. In the second approach, solid sodium chloride particles are added to the aerosol stream. These particles serve as sinks for water vapor and give rise to evaporation of the saline droplets. Hygroscopic size changes involve two-way coupled mass and heat transfer between the dispersed droplets and their surrounding air. These size changes are simulated by numerical solution of the governing mass and heat transfer equations. The results indicate that the two approaches are

effective in terms of decreasing unwanted deposition in the extra-thoracic airways, while increasing deposition in the alveolar regions of the lung (Javaheri and Finlay, 2013).

4.2 Methodology

4.2.1 Problem description

A challenge in respiratory drug delivery is to transport the pharmaceutical particles through the upper airways and deliver them to the target areas in the lung. The deposition site of these particles is mainly determined by their size. Nevertheless, inhalers do not necessarily optimize the particle size. However, if particles undergo controlled size changes, more favorable sizes may be obtained. In particular, for volatile droplets, this could be performed via hygroscopic size changes, which are controlled by adjusting the temperature and relative humidity of the aerosol stream. Nebulizers typically produce aerosol where the vapor concentration at the surface of droplets equals that in the bulk gas (Stapleton and Finlay, 1995), which is a state of vapor pressure balance. The HA and EA processes are aimed at breaking this equilibrium and starting evaporation.

To explore the possibility of HA and EA processes, here we assume that the nebulizer provides an aerosol stream with a volume flow rate of 18 l/min, containing polydisperse saline droplets with mass median diameter (MMD) of 6 μm and geometric standard deviation (GSD) of 1.7. These are typical values at the mouthpiece of jet nebulizers. These droplets are assumed to be initially isotonic, i.e. the concentration of the NaCl in the saline droplets is 9 mg/ml. The total volume of the

delivered droplets is assumed to be 0.5 ml/min. This is a relatively high nebulizer output and corresponds to a relatively high mass concentration of the droplets. For this case, the impact on the surrounding gas by the dispersed droplets (two-way coupling) is significant. At the nebulizer output, the temperature of the aerosol stream and the RH of the carrier air are assumed to be 20°C and 99.5%, respectively. This corresponds to a state of mass balance between the isotonic saline droplets and their surrounding air.

During HA and EA processes, the nebulizer output is passed through a cylindrical chamber, which provides sufficient residence time for the shrinkage of droplets. This chamber will be referred to as the heating chamber in the HA process and as the mixing chamber in the EA process. The diameter and length of the chamber are chosen to be 7 cm and 25 cm, respectively. The average residence time of droplets in the chamber is estimated to be 3.2 sec, which is the ratio of the volume of the chamber by the volume flow rate of the air. During the HA process, a uniform heat flux of 400 W/m^2 is imposed on the lateral surface of the heating chamber. During the EA process the walls of the mixing chamber are adiabatic but the nebulizer output is assumed to be mixed with solid NaCl particles. These particles are also assumed to be polydisperse, with MMD of 1 μm and GSD of 1.7. The total inhaled amount of the added salt particles is assumed to be 9 mg/min.

Our goal is to investigate the dynamics of droplet shrinkage by numerical analysis of the governing mass and heat transfer equations, and determine the size of the droplets resulting from the HA and EA processes. The effectiveness of these processes will be assessed based on the deposition characteristics of the resultant droplets in the respiratory tract.

4.2.2 Governing equations

In order to treat the transport of mass and heat between the dispersed droplets and the carrier air, lognormal size distributions for the saline droplets as well as the salt particles (in EA process) are discretized into N=100 evenly spaced size bins of width 0.2 μm, in the range between 0 and 20 μm. Differential equations of mass and heat transfer govern the diameter d_i and temperature T_i of the droplets in the ith size bin. These equations are discussed in detail by several authors (Fuchs, 1959; Mason, 2010; Seinfeld and Pandis, 2006; Finlay, 2001) and are given here for the sake of clarity and completeness.

The diameter (d_i) of the ith saline droplet size and that of the ith salt particle size are governed by an equation of mass transfer:

$$\frac{\mathrm{d}d_i}{\mathrm{d}t} = \frac{-4\,D\,(C_i - C_\infty)}{\rho_w\,d_i} \tag{4.1}$$

where D is the coefficient of diffusion of water vapor in the air and ρ_w is the density of the liquid water. C_i is the water vapor concentration at the surface of the ith droplet/particle size and the subscript ∞ denotes the bulk air. For solution droplets, the water vapor concentration at the surface is less than that for droplets of pure water. In contrast, the surface curvature tends to increase the vapor concentration at the surface (via the Kelvin effect). For the present saline droplets, these effects are formulated using the correlations given by Cinkotai (1971).

The behavior of salt particles depends on the RH of their surrounding air. At low RH values, NaCl particles remain solid. As the RH increases, at a threshold value, which is characteristic of the particle composition, the solid particle spontaneously

absorbs water, producing a saturated aqueous solution. The RH value at which this phase transition occurs is known as the *deliquescence relative humidity* (DRH). The DRH of NaCl at 298 K, for a flat interface of gas-solid, is 75.3% (Seinfeld and Pandis, 2006; Cinkotai, 1971; Kim et al., 1993). This equals the value of the RH at the surface of the saturated saline and also at the surface of the solid sodium chloride. Further increase of the RH leads to condensational growth of the salt particles. In the present study, because the NaCl particles are mixed with air at 99.5% RH, condensational growth starts immediately after mixing. Therefore, what is referred to as a salt particle is so only at time zero. This designation is used only to distinguish between initially solid particles and initially saline droplets.

The temperature (T_i) of the ith saline droplet size and that of the ith salt particle size are governed by an equation of heat transfer:

$$\rho\, c_p\, \frac{{d_i}^2}{12}\, \frac{\mathrm{d}T_i}{\mathrm{d}t} = -L\, D\, (C_i - C_\infty) - \kappa\, (T_i - T_\infty) \tag{4.2}$$

Here, ρ and c_p are respectively the density and specific heat of the saline droplet or salt particle. L is the latent heat of evaporation of the liquid water which is assumed to be independent of temperature and κ is the thermal conductivity of the air.

During shrinkage and growth, saline droplets and salt particles act as sources/sinks of water vapor and heat. In the temperature range of 10-40°C, the water vapor content of the air varies between 0-51 g/m^3, depending on the relative humidity. As a result, when the order of magnitude of the mass concentration of the saline droplets is 10 g/m^3, the thermodynamic state of the carrier air is expected to be influenced by the hygroscopic size change of the dispersed droplets. Differential equations

governing the temperature and vapor content of the air are as following:

$$\rho_a \, c_{p_a} \frac{\mathrm{d}T_\infty}{\mathrm{d}t} = \frac{4 \, \dot{q}''}{D_c} + \sum_i 2 \, \pi \, \kappa \, n_i \, d_i \, (T_i - T_\infty) \tag{4.3}$$

$$\frac{\mathrm{d}C_\infty}{\mathrm{d}t} = \sum_i 2 \, \pi \, D \, n_i \, d_i \, (C_i - C_\infty) \tag{4.4}$$

Here, ρ_a and c_{p_a} are the density and specific heat of the air, respectively. D_c is the diameter of the chamber and $\dot{q}''$ is the heating power per unit area from the lateral surface of the chamber, which is zero during the EA process. n_i is the number concentration of the particles in the ith size bin. In the HA process, the summations are over the saline droplets while in the EA process the summations are over the both saline droplets and salt particles.

4.2.3 Numerical solution

Equations (4.1) to (4.4) represent a set of nonlinear, coupled, ordinary differential equations governing the diameter and temperature of the particles as well as the the temperature and vapor content of the air, as functions of time. Finlay and Stapleton (1995) and Stapleton et al. (1994) numerically validated this mathematical model for both small and large number of droplets per unit volume, while Saleh and Shihadeh (2007) provided experimental validation. Depending on the process under consideration, the actual number of equations varies, i.e. the HA and EA processes comprise 2N+2 and 4N+2 equations, respectively.

Because of the wide range of characteristic times, the set of eqs. (4.1) and (4.2) is moderately stiff. Therefore, the CVODE routine of the Lawrence Livermore

National Laboratory, Numerical Mathematics Group (Cohen and Hindmarsh, 1994) is used. The underlying integration method implemented in CVODE is a variable order Backward Differentiation Formula (BDF), an implicit scheme with satisfactory stability for stiff ODEs. To validate the numerical analysis, the ODE system was also solved with the aid of an in-house developed code, using the explicit Runge-Kutta-Fehlberg (RKF45) algorithm, with adaptive variable size time step (Burden and Faires, 2010). Due to excessively small time steps, the run time for the RKF45 was considerably higher compared with the implicit BDF.

The deposition of the droplets upon entry into the respiratory tract is calculated using the approach of Javaheri et al. (2013b), which is a modification of the procedure outlined by Finlay and Stapleton (1995). This involves calculating droplet sizes, as well as continuous phase temperature and humidity, as the aerosol transports through each generation of an idealized one-dimensional respiratory tract model. Deposition in each lung generation is estimated using well known equations for impaction, sedimentation and diffusion (Finlay, 2001).

4.3 Results and discussion

4.3.1 The HA process

During the HA process, the aerosol stream delivered by the nebulizer is uniformly heated within the heating chamber. The temperature of the aerosol stream increases. This gives rise to an increase in the concentration of the water vapor at the surface of the saline droplets. Thus, evaporation starts. The provided thermal energy is mainly consumed by latent heat of evaporation. Figure 4.1 illustrates the variations

of relative humidity and temperature of the carrier air as functions of transit time through the heating chamber.

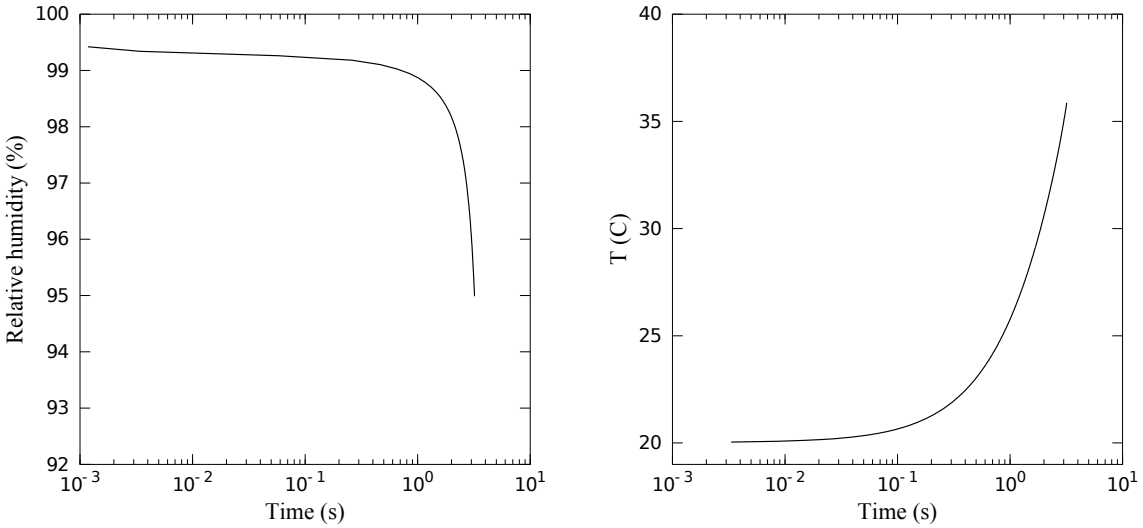

Figure 4.1: The variations of relative humidity and temperature of the air *vs.* the time of transit through the heating chamber

Figure 4.1 indicates that two different phases can be distinguished during the HA process: In the first phase, the rate of variation of RH and temperature is slow. In this phase, the provided thermal energy mainly supplies the latent heat of evaporation of the droplets. When the moisture content of the continuous phase is constant, RH decreases by heating. In the case of the HA process, however, evaporation of droplets partially compensates this effect and prevents much change in RH. Indeed, evaporation moderates the rate of increase of temperature, as well as the rate of decrease of RH. In the second phase, the rate of variation of RH and temperature is fast. In this phase, the shrunk droplets have lost most of their water content and can no longer influence the thermodynamic state of their surrounding air. Thus, the provided thermal energy warms up the air. This gives rise to a rapid increase in temperature and a rapid decrease in relative humidity.

The variations of the diameter of droplets, normalized by the initial diameter, as a function of time of transit through the heating chamber, is given in Fig. 4.2. The trend of shrinkage of droplets corresponds to the trend of variation of RH and temperature of the air, i.e. the two aforementioned phases of the HA process could be recognized on the curves of Fig. 4.2.

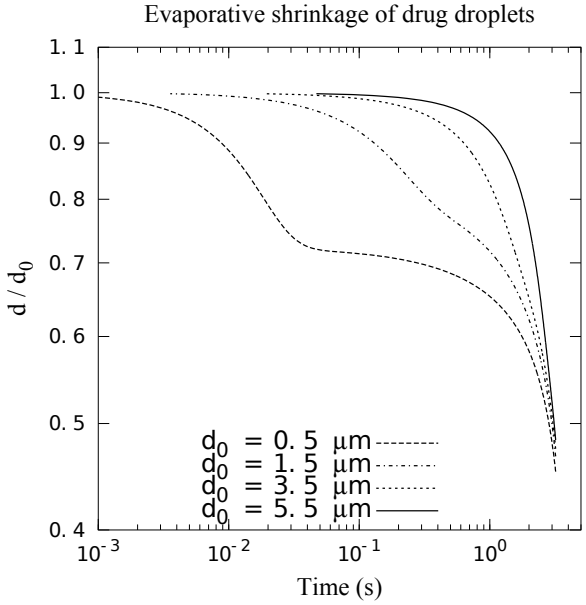

Figure 4.2: The variations of normalized diameter of the different droplet sizes *vs.* the time of transit through the heating chamber

Figure 4.2 also indicates that small droplets evaporate much faster than the large ones, since the characteristic time of evaporation is proportional to the inverse square of the droplet diameter (see eq. (4.1)). During the HA process, the trend of the variation of the temperature of the droplets exactly follows that of air. However, air temperature is always a little bit higher than droplet temperature. This trivial temperature difference is the driving force for heat transfer from air to droplet. The transfered heat partly increases the temperature of the droplet and partly supplies the latent heat of evaporation.

4.3.2 The EA process

During the EA process, the walls of the mixing chamber are assumed to be adiabatic and the size of the saline droplets is controlled by adding excipient sodium chloride particles. This process comprises evaporation of the saline droplets as well as condensational growth of the salt particles, associated with corresponding changes in temperature and vapor content of the carrier air. The variations of the diameter of the saline droplets and salt particles, normalized by the initial diameter, as functions of time of transit through the mixing chamber, are given in Fig. 4.3.

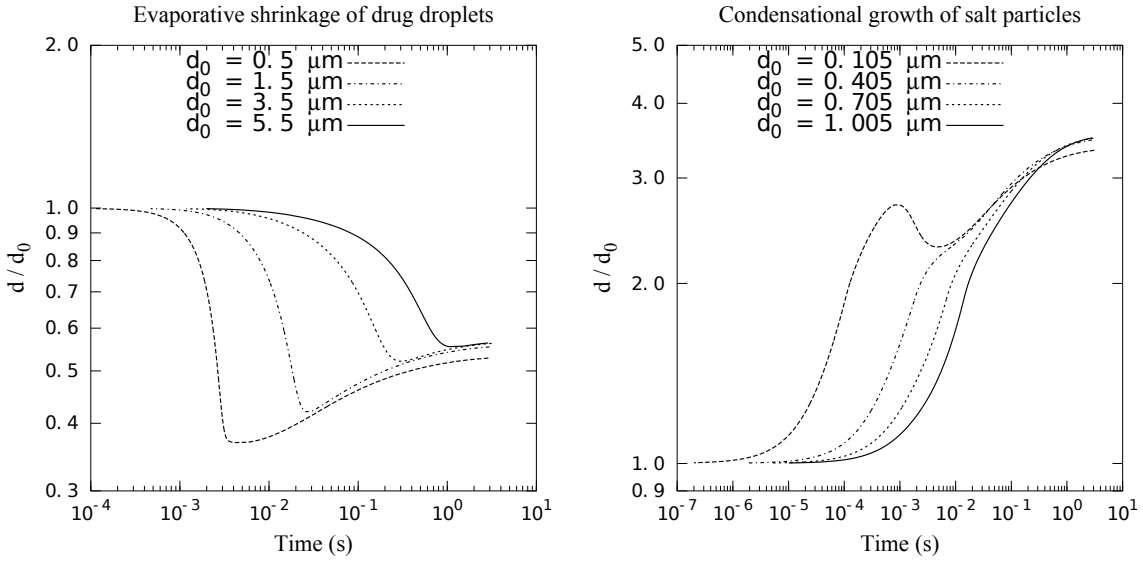

Figure 4.3: The variations of normalized diameter of the saline droplets (left) and salt particles (right) *vs.* the time of transit through the mixing chamber

Figure 4.3 confirms that evaporation of the saline droplets occurs subsequent to the growth of the salt particles. At the end of the EA process, a state of mass balance is reached, i.e. the vapor pressure at the surface of all of the droplets and that of the surrounding air are the same. This implies that the mass concentration of NaCl in all the resultant droplets should be nearly the same, although not exactly

the same because of the Kelvin effect. Note that the addition of the salt results in the initially isotonic droplets becoming hypertonic upon exiting the mixing chamber, with a concentration of (50-55 mg/ml), which is a concentration in the range used in the treatment of certain pulmonary diseases (Elkins and Bye, 2006).

The variations of relative humidity and temperature of air during the EA process are given in Fig. 4.4 as functions of time of transit through the mixing chamber. In accord with Fig. 4.3, Fig. 4.4 also confirms that the growth of the salt particles occurs prior to the evaporation of the saline droplets. In the first stage of the EA process, when the condensational growth dominates, the RH of the air decreases, and because condensation is a heat generating process, the temperature of the air increases. In the second stage, the trend is reversed, i.e. evaporation dominates, the RH of the air increases and the temperature decreases. The final temperature in the EA process is higher than the initial temperature. Given that this process is adiabatic, this means that the total mass of the condensed vapor is more than the total mass of the evaporated water.

4.3.3 Deposition in the respiratory tract

The goal of the both HA and EA processes is to manipulate the size of the saline droplets and produce smaller droplets which are more appropriate for drug delivery to the lungs. Therefore, the effectiveness of these processes is evaluated by determining the deposition characteristics of their resultant droplets. The droplets produced during the HA and EA processes will continue their size change after inspiration. The shrunken droplets absorb water vapor and undergo condensational growth during their progress through the thoracic airways. Our simulations show that these

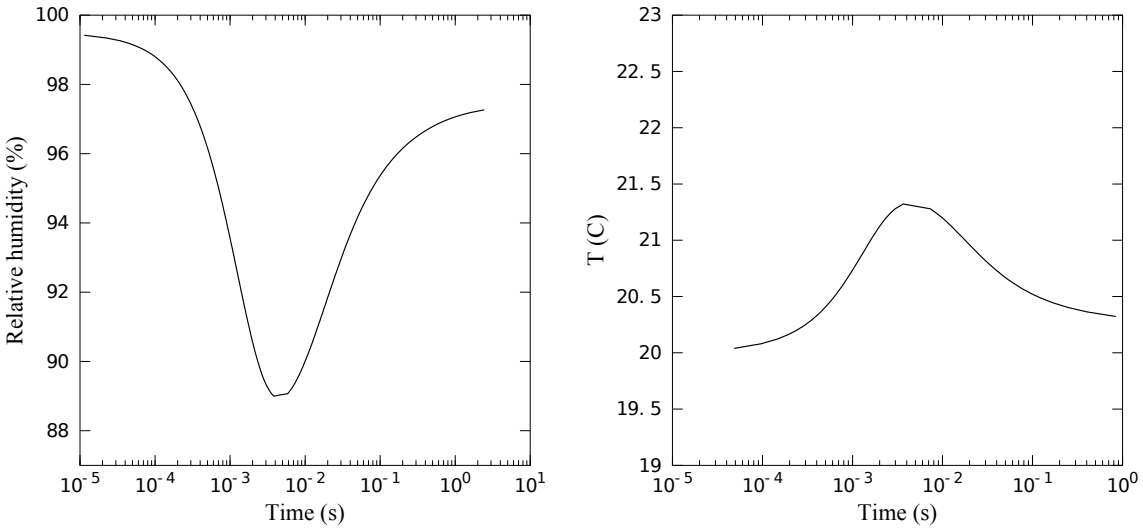

Figure 4.4: The variations of relative humidity and temperature of the air *vs.* the time of transit through the mixing chamber

droplets grow sufficiently not to be exhaled for the parameter ranges considered here. In the alternative size manipulation approaches of Hindle and Longest (2010) and Longest et al. (2012b), (ECG and EEG), submicrometer particles pass through the extrathoracic airways, and undergo a controlled condensational growth when advancing through the thoracic airways.

	Extra-thoracic	Tracheo-Bronchial	Alveolar
Fractional deposition of nebulizer output	21.9%	27.2%	33.5%
Fractional deposition of HA processed droplets	8.9%	19.6%	48.4%
Fractional deposition of EA processed droplets	7.2%	20.4%	48.7%

Table 4.1: Deposition of the droplets produced in HA and EA processes compared to deposition of the unaltered nebulizer output.

The regional deposition of HA and EA processed droplets is calculated using the methodology explained in Javaheri et al. (2013b). The results are summarized in

Table 4.1. Based on the deposition data of Table 4.1, the HA and EA processes can enhance deep lung deposition of the nebulized saline droplets: alveolar deposition improves by 45% increase, while extra-thoracic deposition decreases 59% in the HA process and 67% in the EA process. Despite these noteworthy improvements, implementation of the HA and EA processes is an issue by itself. Laboratory implementation of the HA process seems straightforward: the thermal energy could be supplied by an electric resistance heater wrapped around the lateral surface of a heating chamber. In the HA process, once the dispersed droplets were fully evaporated, the steep increase of temperature is a major consideration (see Fig. 4.1). Longest et al. (2012a) considered different methods of providing thermal energy. Uniform heat flux, or a wire type wall heater were found to be unsafe for direct inhalation, while a counter-flow heater design (Longest et al., 2012a, 2013) provided more control over temperature. The EA process, however, may not be straightforward to implement. A separate device, synchronized with the nebulizer is needed to appropriately add the salt particles to the aerosol stream. The goal of this study does not involve addressing these issues.

5. Numerical Simulation of Flocculation and Transport of Suspended Particles: Application to Metered-Dose Inhalers

5.1 Introduction

This Chapter investigates the dynamics of flocculation and convective transport of solid particles suspended in a liquid propellant (Javaheri and Finlay, 2014), within the canister of a pressurized metered-dose inhaler (MDI). Polydisperse particles with lognormal size distribution are considered. Collision of particles is presumed to be controlled by two mechanisms: upward velocity differential, which is schematically illustrated in Fig. 5.1, and Brownian motion. These mechanisms are enhanced by the van der Waals force. Flocculation of the particles is described using the continuous form of the Smoluchowski equation. Flocculation produces larger particles with higher upward velocity. Upward transport of the particles is specified via a convection term. A schematic of phase separation and formation of a cream layer at the surface of the propellant due to the upward drift of the particles is depicted in Fig. 5.2. The general dynamics of the system is governed by a nonlinear transient partial integro-differential equation which is solved numerically. The technique employed is based on discretizing the size distribution function using orthogonal col-

location on finite elements. This is combined with a finite difference discretization of the physical domain, and an explicit Runge-Kutta-Fehlberg time marching scheme. The numerical analysis is validated by comparing with a closed form analytical solution. The simulation results represent the particle size distribution as a function of time and position. The method allows prediction of the effects of the initial conditions and physical properties of the suspension on its dynamic behavior and phase separation.

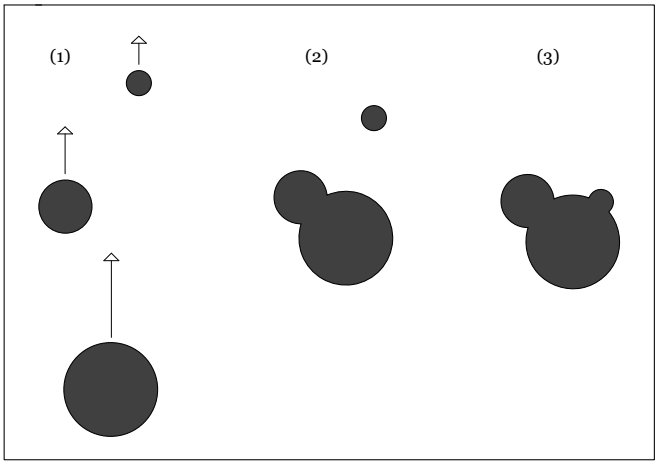

Figure 5.1: Schematic of collision of particles by upward velocity differential.

5.2 Methodology

5.2.1 Mathematical formulation

Within the canister, particles flocculate and simultaneously drift upward. These two processes are not independent, i.e. flocculation generates larger particles with higher drift velocity. This increases the rate of collision of upward moving particles, thereby accelerating flocculation. The mathematical model governing this dynamics

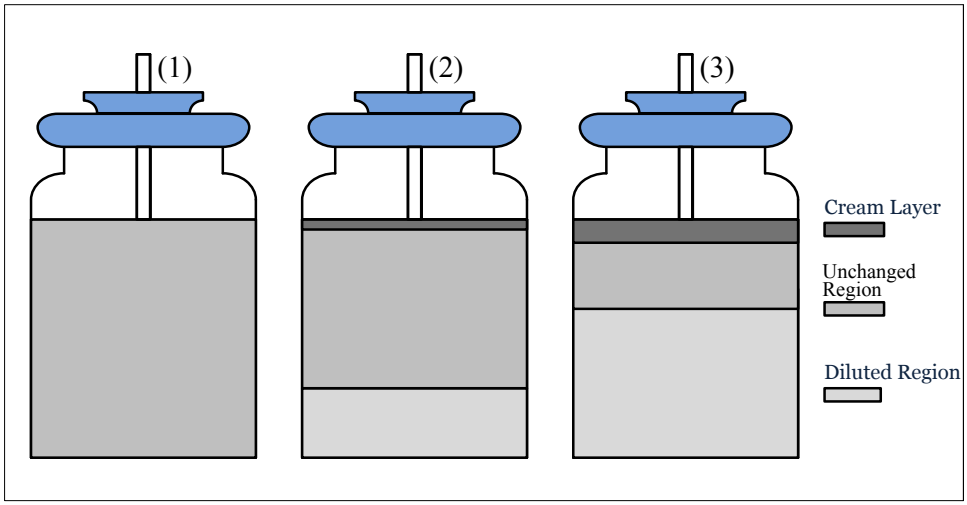

Figure 5.2: Schematic of an MDI canister at 3 subsequent points (1), (2), and (3) in time, showing phase separation and formation of a cream layer at the surface of the propellant.

is a reduced form of the GDE, and is given by

$$\frac{\partial n(d,z,t)}{\partial t} + \frac{\partial \left(U_d \, n(d,z,t) \right)}{\partial z} = \frac{d^2}{2} \int_0^d \frac{\beta(\tilde{d},\varphi)}{\varphi^2} \, n(\varphi,z,t) \, n(\tilde{d},z,t) \, d\tilde{d} \\ - n(d,z,t) \int_0^\infty \beta(d,\tilde{d}) \, n(\tilde{d},z,t) \, d\tilde{d} \tag{5.1}$$

in which $\varphi = (d^{\,3} - \tilde{d}^{\,3})^{1/3}$ and $n(d,z,t)$ is the size distribution function, where $n(d,z,t)\mathrm{d}d$ is the number of particles per unit volume of propellant, at location z and time t, having diameters in the range d to $d+\mathrm{d}d$. Here z is the vertically upward distance from the canister bottom, and we assume no spatial variation in other directions. The flocculation of particles is formulated using the continuous form of the Smoluchowski equation (Friedlander, 2000). The flocculation kernel, $\beta(d,\tilde{d})$, is determined by the mechanisms of particle collision. The upward drift of particles is described by the convection term on the left hand side. U_d is particle

drift velocity, and is given by

$$U_d = (1 - V_{fr})^{6.0}\, \Lambda\, \frac{g\, d^2}{18\, \mu} \tag{5.2}$$

where V_{fr} is the volume fraction of particles in the suspension. The term $(1 - V_{fr})^{6.0}$ represents a hindrance function and takes into account the effect of concentration on drift velocity (Russel et al., 1992); $\Lambda = (1 - \phi)\,(\rho_f - \rho_t)$ is an effective density difference in which ϕ is the porosity of the particles and ρ_f and ρ_t are the density of the propellant, and the true density of the particle, respectively. Finally, g is gravitational acceleration and μ is the dynamic viscosity of propellant.

To render the problem tractable, the following assumptions and simplifications are also made:

- Particles are initially spherical. Moreover, the flocs built up by the collision and aggregation of particles are also spherical. In reality, flocs are not necessarily spherical and their geometrical characteristics are specified by defining equivalent diameters (Jarvis et al., 2005). However, considering the effects of floc fractal dimensions on the rate of flocculation is beyond the scope of the present study.
- When particles collide, they remain attached to each other with a presumed efficiency, which is equal to 100% for the current simulation.
- The frequency of particle collision is controlled by two mechanisms: upward velocity differential and Brownian motion. These mechanisms are enhanced by the van der Waals force. The electrostatic repulsion potential is thought to be insignificant in the propellant media (Albers and Overbeek, 1959a,b; Chen and

Levine, 1973; Féat and Levine, 1975, 1976; Johnson, 1996). This is attributed to the relatively large ratio of double layer thickness to inter-particle separation distance in non-aqueous media (Albers and Overbeek, 1959b; Johnson, 1996). The repulsion potential also strongly diminishes when the volume fraction of particles is not extremely low (Albers and Overbeek, 1959b). Assuming additivity of the rates of collision by the different mechanisms, the flocculation kernel for two particles with diameters d_1 and d_2 can be expressed (Friedlander, 2000; Williams and Loyalka, 1991; Seinfeld and Pandis, 2006; Jacobson, 2005) as

$$\beta(d_1, d_2) = \left(\frac{2\, k_B\, T}{3\, \mu} (\frac{1}{d_1} + \frac{1}{d_2}) (d_1 + d_2) \right) / W + (U_{d_1} - U_{d_2}) \frac{\pi}{4} (d_1 + d_2)^2 \quad (5.3)$$

where the first term specifies the effect of Brownian motion and van der Waals force. The latter appears in the denominator and is given by Friedlander (2000):

$$W = \int_0^1 exp\left(-\Upsilon \left[\frac{1-\Psi}{12} (\frac{x^2}{1-x^2} + \frac{x^2}{1-\Psi\, x^2}) + \frac{1}{6} \ln(\frac{1-x^2}{1-\Psi\, x^2}) \right] \right) dx \quad (5.4)$$

in which $\Psi = (d_1 - d_2)^2/(d_1 + d_2)^2$ and $\Upsilon = A/k_B T$ where A is the Hamaker constant, k_B is the Boltzmann constant, and T is temperature. The value of the Hamaker constant is not reported for drug particles in liquid propellants. However, the value of $A = 10^{-20}$J which is used here lies in the range for the solid particles dispersed in liquids (Tadros, 2012). Flocculation kernel is not very sensitive to the Hamaker constant (Friedlander, 2000). Nevertheless, the right value of Hamaker constant is needed for more accurate results. The second term in Eq. (5.3) specifies the effect of upward velocity differential,

i.e. collision of particles moving upward with different velocities (see Fig. 5.1) (Seinfeld and Pandis, 2006).

It is to be noted that the applicability of the current numerical method does not depend on the mathematical form of the flocculation kernel, i.e. the kernel may be modified to account for some neglected effects, and the method will be still applicable. However, if the nature of the inter–particle forces is very different from what is considered here, the results of the current simulation may not agree well with experimental observations.

The bottom of the canister is the location where phase separation appears first (see Fig. 5.2). The dose of the drug is also usually taken from that place. Thus, even in its first stages, phase separation interferes with the consistency of drug delivery. In order to investigate this phenomenon quantitatively, the characteristic time of phase separation is defined to be the time, T_{ps}, when the volume fraction of particles at the bottom is reduced by 50%.

5.2.2 Numerical approach

Equation (5.1) is a nonlinear transient partial integro-differential equation. Overall, this equation cannot be solved analytically. Thus, a numerical approach is needed. Equation (5.1) is comprised of three different parts: the time derivative on the left hand side, the first order position derivative (convection term) on the left hand side, and the integrals on the right hand side. Each term can be tackled using a particular numerical scheme. The integrals on the right hand side, which specify the flocculation of particles at a particular time and position, are the most challenging terms. These integrals are discretized using a combination of orthogonal collocation

on finite elements (Carey and Finlayson, 1975), and Gauss-Legendre quadrature. The application of orthogonal collocation on finite elements for particulate systems is elucidated by Gelbard and Seinfeld (1978).

In order to discretize the size distribution function, the diameter domain is assumed to be finite, with boundaries d_{min} and d_{max}. Depending on the initial size distribution, d_{min} and d_{max} are set to span at least three orders of magnitudes of particle diameters, e.g. $d_{min} = 0.1\,\mu m$ and $d_{max} = 100\,\mu m$. This essentially eliminates the so-called finite-domain error (Gelbard and Seinfeld, 1978). The diameter domain is divided into M elements. The size of elements is not uniform, i.e. smaller elements in small diameter ranges, and larger elements in large diameter ranges. The elements represent a geometric sequence with a common ratio between 1.02 to 1.05, depending on the initial GSD (geometric standard deviation) of the particles. Each element has two interior collocation points, taken as the roots of the shifted Legendre polynomial. The values of the distribution function are to be determined at each collocation point (not the grid points), at any time and position. Within each element, the diameter is scaled from 0 to 1 to reduce round-off error. The distribution function, $n(d, z, t)$, is also represented using a cubic polynomial.

$$n_i(d, z, t) = a_{i,0}(z, t) + a_{i,1}(z, t)X_i + a_{i,2}(z, t)X_i^2 + a_{i,3}(z, t)X_i^3 \quad i = 1, 2, ...M \quad (5.5)$$

in which $n_i(d, z, t)$ is the distribution function on the ith element and $X_i = \frac{d - d_{i-1}}{d_i - d_{i-1}}$. Once the collocation points are scaled, $X_{c1} = \frac{1}{2}(1 - \frac{1}{\sqrt{3}})$ and $X_{c2} = \frac{1}{2}(1 + \frac{1}{\sqrt{3}})$ will be the same on all the elements. The values of the distribution function and the cubic

polynomials are equal at the collocation points.

$$n(d_{c_{i,j}}, z, t) = a_{i,0}(z,t) + a_{i,1}(z,t)X_{cj} + a_{i,2}(z,t)X_{cj}^2 + a_{i,3}(z,t)X_{cj}^3 \qquad (5.6)$$
$$j = 1, 2 \qquad i = 1, 2, ...M$$

where $d_{c_{i,j}}$ is the diameter of the jth collocation point on the ith element. Moreover, at the grid points between elements, the left and right polynomials as well as their first derivatives are forced to be continuous, i.e.

$$a_{i,0}(z,t) + a_{i,1}(z,t) + a_{i,2}(z,t) + a_{i,3}(z,t) = a_{i+1,0}(z,t) \qquad (5.7)$$

$$a_{i,1}(z,t) + 2\,a_{i,2}(z,t) + 3\,a_{i,3}(z,t) = \frac{d_i - d_{i-1}}{d_{i+1} - d_i}\,a_{i+1,1}(z,t) \qquad (5.8)$$

The boundary conditions of the diameter domain take the form

$$a_{1,0}(z,t) = 0 \quad and \quad a_{M,0}(z,t) + a_{M,1}(z,t) + a_{M,2}(z,t) + a_{M,3}(z,t) = 0 \qquad (5.9)$$

Equations (5.6) to (5.9) can be solved for the 4M unknown coefficients of the M cubic polynomials. Once the coefficients are determined, the integrals in Eq. (5.1) can be calculated using Gauss-Legendre quadrature, i.e. the right hand side of Eq. (5.1) is evaluated for all the 2M collocation points.

On the left hand side of Eq. (5.1), the convection has a hyperbolic nature and describes the upward transport of the particulate phase. Because of the small values of the drift velocity, upwinding is not a concern here and the convection term is discretized using a second order finite difference method (Patankar, 1980). Along the z-axis of symmetry of the canister geometry, the physical domain of the particle-

propellant system is discretized into N uniformly spaced grid points. The time step for explicit time marching, demanded by the convection term, can be estimated using the CFL (Courant-Friedrichs-Lewy) condition, based on the Courant number (LeVeque, 2002):

$$\frac{U_d \, \Delta t}{\Delta z} < C_{max} \tag{5.10}$$

where Δz is the grid size, and C_{max} is the maximum allowed Courant number. The maximum value of U_d, corresponding to the largest flocs which may appear in the canister, is of order of magnitude 1 mm/sec. The order of magnitude of the grid size is 1 mm, and C_{max} is set to be 1. Therefore, the time step demanded by the CFL condition is of order of magnitude of 1 sec. The CFL condition provides an upper bound for the time step.

The time scale of flocculation does not remain constant throughout the evolution of the process. It is short at the beginning, but when the size distribution approaches a steady state, the time scale approaches infinity. In contrast, the time scale of convection has its maximum value at the beginning, and becomes shorter as larger particles gradually appear in the canister. Due to the marked changes of time scale, normally by two orders of magnitude, the first order time derivative on the left hand side of Eq. (5.1) needs special treatment. The fourth order - fifth order Runge-Kutta-Fehlberg (RKF45) (Atkinson et al., 2011; Burden and Faires, 2010) is an appropriate scheme for this purpose. RKF45 adaptively adjusts the time steps so that the estimated relative error falls between two prescribed bounds. Here, the minimum and maximum values for the relative error are set to be 10^{-5} and 10^{-4}, respectively.

To implement the numerical approach, an in-house C program was developed. To investigate grid independence of the results, two different size computational grids were considered. One with M=150 and N=75, and another one with M=200 and N=100. The variation of the volume fraction of particles at the canister bottom was calculated as a function of time, using the two grids. The differences between the results were observed to be less than 3.5% during the first six minutes of evolution of the process.

5.2.3 Validation of the numerical approach

In the absence of the convection term, numerical solution of Eq. (5.1) can be validated against an analytical solution (Scott, 1968; Gelbard and Seinfeld, 1978). Since the mathematical model of flocculation poses the greatest numerical challenge whereas the convection term does not pose any numerical difficulty, validation of the numerical solution of Eq. (5.1) in the absence of the convection term is worthwhile.

To obtain an analytical solution, an exponential initial size distribution is considered:

$$\bar{n}(\bar{d}, 0) = 3\,\bar{d}^{\,2}\,exp(-\bar{d}^{\,3}) \tag{5.11}$$

in which $\bar{d} = d/d_0$ where d_0 is the mean initial diameter. Also $\bar{n} = n\,d_0/N_0$ where N_0 is the total initial number concentration of particles. Assuming a constant flocculation kernel, $\beta = \beta_0$, analytical solution of the flocculation equation for

initial distribution of Eq. (5.11) is given as the following:

$$\bar{n}(\bar{d},\tau) = \frac{12\,\bar{d}^{\,2}}{(\tau+2)^2}\,exp\left(\frac{-\bar{d}^{\,3}}{\tau+2}\right) \tag{5.12}$$

where $\tau = N_0\beta_0 t$ is the dimensionless time.

To demonstrate the validity of the present approach, the evolution of the size distribution of Eq. (5.11) is numerically simulated, using M=150 elements. The results of the simulation along with the analytical solution of Eq. (5.12) are depicted in Fig. 5.3. Excellent agreement between the numerical and exact solution is obtained. This suggests that the present simulation approach can also be successfully applied to solve Eq. (5.1).

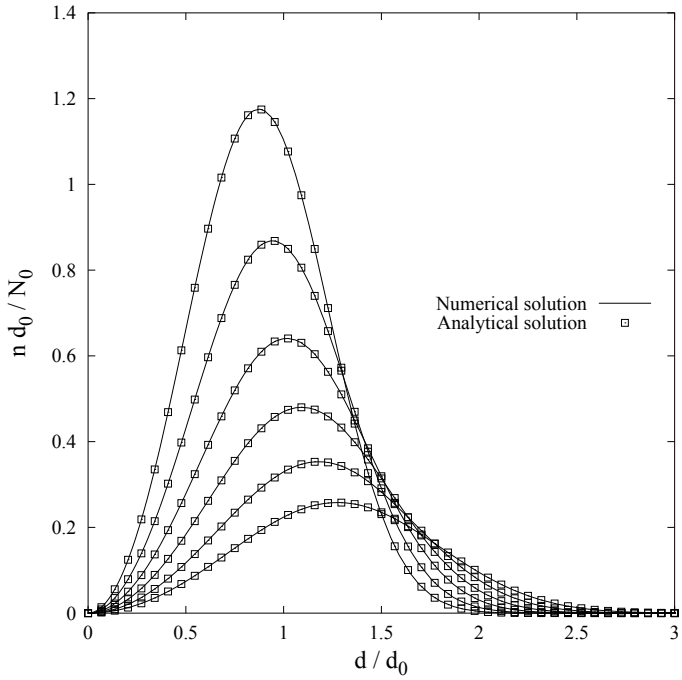

Figure 5.3: Results of the validation run: Numerical solution of Eq. (5.1) in the absence of the convection term is compared with the analytical solution, for particles with an initially exponential size distribution and constant flocculation kernel.

The finite-domain error, which arises from bounding the infinite domain of particle diameter, could potentially give rise to spurious results. In fact, the value of the upper bound of the finite domain, d_{max}, is a major consideration, because that should be higher than the size of the largest particles which may appear in the canister. Our numerical experiments reveal that these large particles remain of the order of magnitude of the initial *MMD*, see e.g. Fig. 5.9 in the next section, while in the computational code, d_{max} is set to be at least 33 times larger than the initial *MMD*. This promises a negligible finite-domain error. A method for quantitative analysis of the finite-domain error in the absence of the convection term is given by Gelbard and Seinfeld (1978).

5.3 Results and Discussion

Inside the canister, the variations of volume fraction and phase separation are affected by several physical parameters. Among these, the effects of the following, which are most relevant to the present mathematical model, are underscored: the initial volume fraction V_{fr_0}, effective density difference Λ, and initial size distribution, i.e. MMD_0 and GSD_0. To demonstrate the current method, the effect of these parameters on the characteristic time of phase separation, T_{ps}, is simulated for nine different cases, and the results are summarized in Table 5.1. The first case is the reference, representing typical values of these parameters, while the other eight cases represent variations of the parameters within their practical range. The parameter values of Table 5.1 are also used in the following illustrations.

The present numerical approach deals with the size distribution function, not the number of particles with a particular size. For monodisperse particles, the

initial size distribution is singular. Instead, in Table 5.1, case 4, monodispersity is approximated by a narrow size distribution with initial GSD of 1.02.

Case	V_{fr_0}	$\Lambda(\frac{kg}{m^3})$	MMD_0 (μm)	GSD_0	T_{ps} (s)
1	0.03	150	2.0	1.5	71.5
2	0.03	150	1.0	1.5	74.2
3	0.03	150	3.0	1.5	65.7
4	0.03	150	2.0	1.02	74.3
5	0.03	150	2.0	2.0	43.0
6	0.03	50	2.0	1.5	141.0
7	0.03	300	2.0	1.5	46.2
8	0.01	150	2.0	1.5	99.6
9	0.05	150	2.0	1.5	63.3

Table 5.1: The effects of the initial volume fraction, effective density difference, and initial size distribution on the characteristic time of phase separation.

The evolution of the particulate phase in the canister is a process with a varying time scale. The explicit RKF45 scheme adaptively adjusts its time steps to the time scale. Thus, variations of the time step are an indication of the variations of the time scale, and provide insight into the rate of evolution of the process. The time steps of RKF45 are given in Fig. 5.4 as a function of time for case 2. It is evident that the time step varies by two orders of magnitude. Though the time step demanded by flocculation increases through time, the gradual appearance of large flocs tends to decrease the time step demanded by the convection term. This leads to some fluctuations in the time step after t=30 s, as is illustrated in Fig. 5.4. The maximum time step, however, is always restricted by the CFL condition.

Of particular interest is the bottom of the canister, where the dose is usually

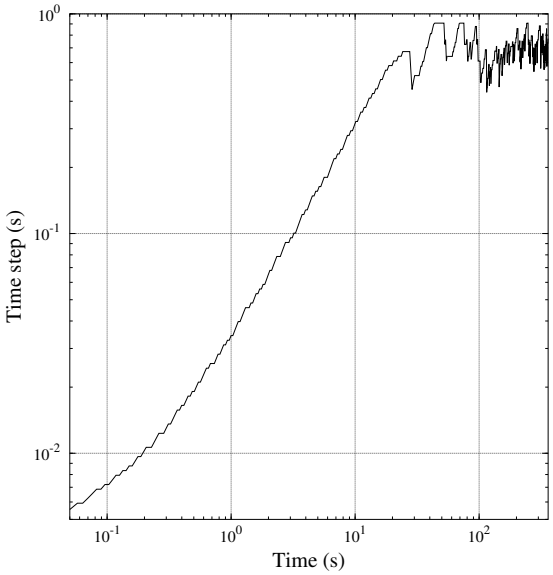

Figure 5.4: Variations of the time step of explicit time marching as a function of time for case 2.

taken. The other place of interest is the surface of the propellant, where drug particles accumulate and build up a cream layer (see Fig. 5.2). The present simulation can predict the variations of the size distribution throughout the canister except at the surface, i.e. the cream layer where the flocs are highly concentrated and the present model of flocculation is no longer valid. Indeed, much larger flocs may appear within the cream layer, compared to those which appear in the bulk of the propellant. Nevertheless, the simulation can still predict the total mass of the particles which accumulate at the surface, since that is governed by convection, not flocculation.

The variations of the normalized volume fraction at the bottom of canister, as a function of time is given in Fig. 5.5. The volume fraction divided by its initial value is referred to as the normalized volume fraction. The variations of the normalized mass accumulated at the surface of the propellant, as a function of time, is given in

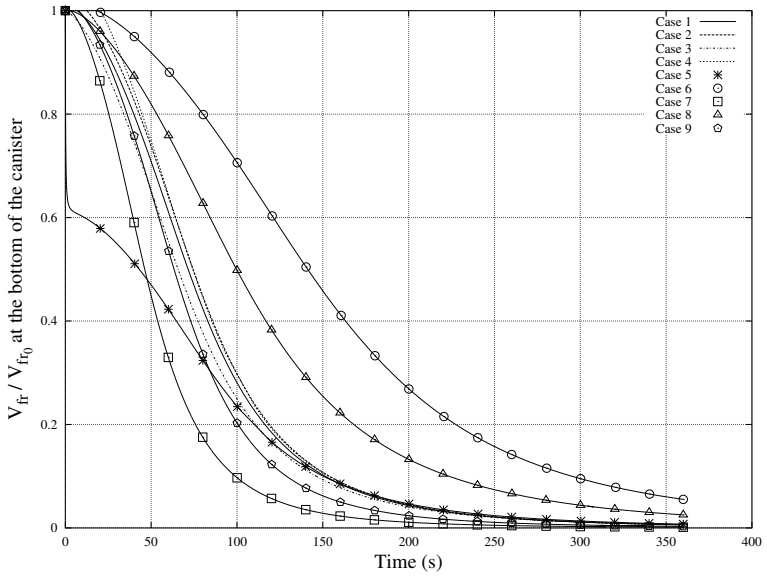

Figure 5.5: Normalized volume fraction vs. time, at the bottom of the canister.

Fig. 5.6. The normalized mass is defined to be the mass of the concentrated cream layer divided by the total mass of the particles in the canister.

All the nine cases listed in Table 5.1 are considered in Fig. 5.5 and 5.6. Both figures make obvious that the effective density difference is the most significant parameter that controls the transport of the particulate phase. This parameter directly contributes to the convection term as well as the flocculation kernel (Eq. (5.1)-(5.3)). In Fig. 5.5, the steep decline of normalized volume fraction for case 5 is due to the rapid migration of the large particles existing in the initial size distribution. Figures 5.5 and 5.6 also illustrate the marked effect of initial volume fraction, and insignificant effect of initial size distribution (except for the case of GSD_0=2.0).

Figure 5.7 illustrates the normalized volume fraction vs. normalized height level at different times, for case 1 in Table 5.1. The normalized height level ($\bar{z}$) is defined to be the height of a position (z) divided by the height of the surface of the

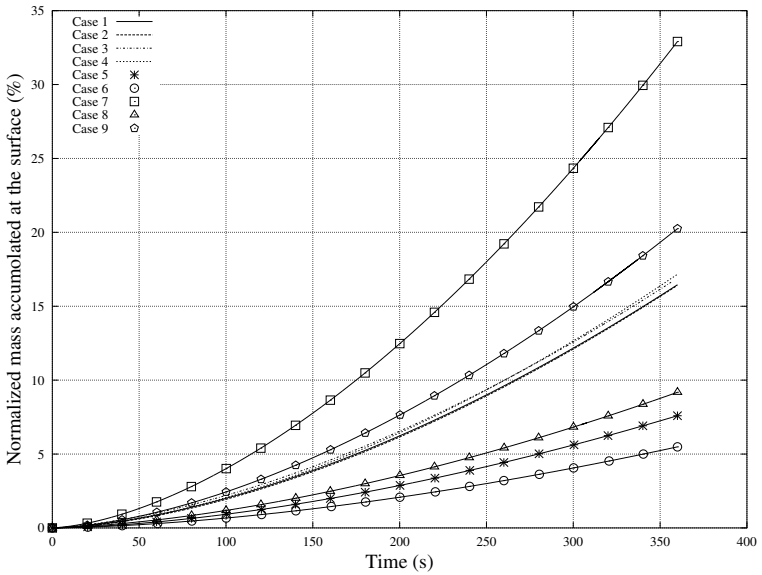

Figure 5.6: Normalized mass accumulated at the surface, as a function of time.

propellant (H), i.e. $\bar{z} = z/H$. The changes in the volume fraction, as depicted in Fig. 5.7, propagate like a wave through different height levels, from the bottom to the top. As a result, at each time, the volume fraction is reduced at some lower levels but remains virtually unchanged at upper levels which have not yet received the wave of diminution. For instance, at t=213 s, the normalized volume fraction at normalized heights higher than 0.2 is almost unchanged. This implies that nearly all the particles that have convected upward accumulate at the propellant surface instead of distributing over levels below the surface. It should be noted that the normalized volume fraction at the propellant surface is not given in Fig. 5.7.

While the normalized volume fraction does not change for sufficiently high z levels, the particle size distribution varies significantly at all levels. For example, Fig. 5.8 depicts the variations of the size distribution of particles through time, at the bottom of the canister, for case 1 in Table 5.1. The results are illustrated

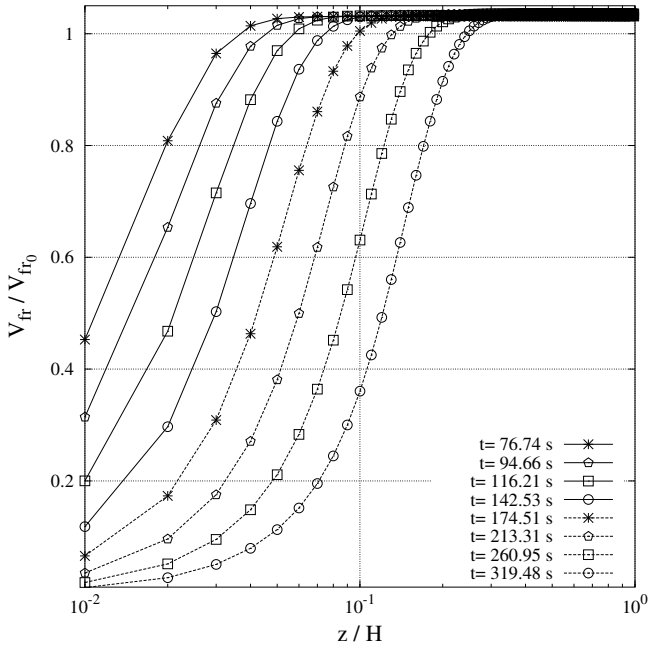

Figure 5.7: Normalized volume fraction vs. normalized height level for case 1.

in terms of dimensionless groups. The independent variable is d/MMD_0, and the dependent variable is $nMMD_0/N_0$ where N_0 is the total initial number concentration of particles. The left panel of Fig. 5.8 depicts the size distribution during the first few seconds, and the right panel depicts that during the first few minutes. These figures illustrate an increase in the average size through the first few seconds, followed by a decrease. The former is because of the flocculation, and the latter is caused by the faster upward migration of the larger particles. Figure 5.9 depicts the variations of the size distribution through time, at the location $\bar{z} = 0.8$, for case 1 in Table 5.1. In this figure, the size distribution initially remains unaffected by the wave of diminution for a relatively long time. Thus, the average size of particles in Fig. 5.9 keeps growing much longer compared to Fig. 5.8.

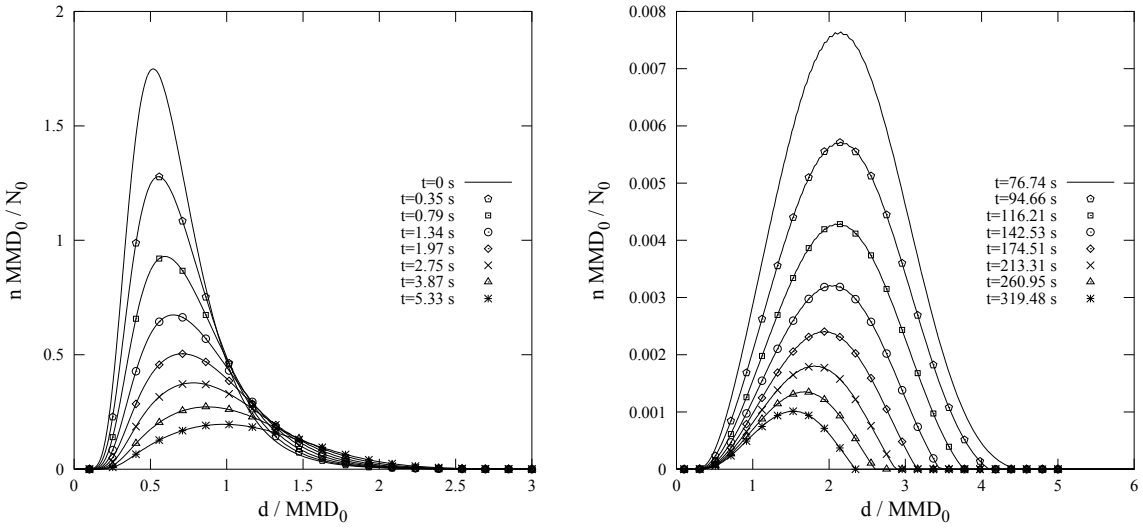

Figure 5.8: Variations of the size distribution at the bottom of the canister for case 1, during the first few seconds (left panel), and first few minutes (right panel).

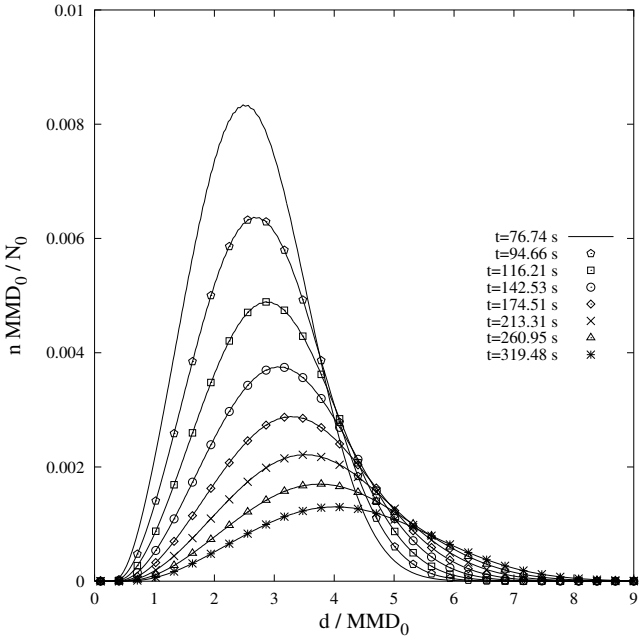

Figure 5.9: Variations of the size distribution at the location $\bar{z} = 0.8$ for case 1, during the first few minutes.

6. Conclusion

An idealized geometry representative of real infant nasal geometries in its aerosol deposition characteristics was introduced in Chapter 2. While real infant nasal airways are morphologically quite complicated, the idealized geometry presented here enjoys the advantage of simplicity. In spite of its fairly simple form, its aerosol deposition agrees with the average of deposition in real airways for 10 subjects in the 3–18 month age range. This geometry is proposed as a possible in vitro reference for examining the lung delivery of aerosols to infants.

The effect of using helium-oxygen instead of air on hygroscopic size changes and deposition of inhaled volatile aerosols was investigated in Chapter 3. The effects of aerosol mass fraction variation were also underscored. Three different values for total inhaled mass of salt (NaCl) per minute, ψ, were examined. The high value of ψ represents the total inhaled salt from a typical high output rate nebulizer, while the low value of ψ represents the case in which hygroscopic size changes are significant. To investigate the differences in He-O_2 and air deposition caused by hygroscopic size changes, the *hygroscopic effectiveness*, λ, was defined. The values of λ confirm that the differences between deposition with helium-oxygen *vs.* air, caused by hygroscopicity, are trivial for high mass fraction, and more noticeable for medium and low mass fractions.

Two size manipulation processes were suggested in Chapter 4, aimed at improving the deposition of nebulized saline aerosols. Each process provides the necessary circumstances for the evaporation and shrinkage of the droplets. In the HA process, the aerosol stream is warmed up. The vapor pressure at the surface of the droplets increases, and evaporation starts as a result. The HA process takes place within a heating chamber. In the second process, EA, solid NaCl particles are added to the aerosol flow. These particles absorb water vapor from the air and result in the evaporation of the saline droplets. The EA process takes place within a mixing chamber. Both the HA and EA processes are shown to produce shrunk droplets with favorable lung deposition characteristics. The results could be useful in the development and design of add-on devices to improve aqueous aerosol drug delivery to the lungs.

In Chapter 5 a simulation approach was presented to model the flocculation and transport of solid particles suspended in a liquid propellant. The collision frequency of particles, and thereby flocculation, was presumed to be influenced by upward velocity differential, Brownian motion and van der Waals force. The repulsive electrostatic force was assumed negligible. The governing mathematical model was a nonlinear transient partial integro-differential equation in which flocculation was described by the Smoluchowski equation and transport of the particles was specified via a convection term. Different terms in the mathematical model were tackled using different numerical schemes. The time derivative was resolved using fourth order - fifth order Runge-Kutta-Fehlberg (RKF45) scheme, the convection term was discretized using a second order finite difference approach, and the flocculation integrals were analyzed using the method of orthogonal collocation on finite elements.

The results specify the evolution of the suspension from an arbitrary initial condition. The influences of the initial volume fraction of particles, effective density difference, and initial size distribution of particles are documented. The results indicate that, compared to the other parameters, the effective density difference has a more pronounced effect on the transport of the particulate phase and phase separation. The present model and numerical approach may be useful to those desiring to understand and predict the behaviors of new and existing MDI formulations for the purpose of improved respiratory drug delivery.

Bibliography

Albers, W., Overbeek, J.T.G., 1959a. Stability of emulsions of water in oil: I. the correlation between electrokinetic potential and stability. Journal of Colloid Science 14, 501–509.

Albers, W., Overbeek, J.T.G., 1959b. Stability of emulsions of water in oil: II. charge as a factor of stabilization against flocculation. Journal of Colloid Science 14, 510–518.

Amirav, I., Newhouse, M.T., 2012. Deposition of small particles in the developing lung. Paediatric Respiratory Reviews 13, 73–78.

Ansys CFX, Release 12.1. help system. ANSYS, Inc.

Ari, A., Fink, J.B., 2010. Aerosol drug administration with helium-oxygen (heliox) mixtures: An overview. Current Respiratory Medicine Reviews 6, 80–85.

Atkinson, K., Han, W., Stewart, D.E., 2011. Numerical solution of ordinary differential equations. Wiley.

Becquemin, M., Swift, D., Bouchikhi, A., Roy, M., Teillac, A., 1991. Particle deposition and resistance in the noses of adults and children. European Respiratory Journal 4, 694–702.

Benjamin, M.M., 2011. Clarification of a common misunderstanding of collision frequencies in the Smoluchowski equation. Journal of Environmental Engineering 137, 297–300.

Bennett, W.D., Zeman, K.L., Jarabek, A.M., 2008. Nasal contribution to breathing and fine particle deposition in children versus adults. Journal of Toxicology and Environmental Health, Part A 71, 227–237.

Bergman, T.L., Incropera, F.P., Lavine, A.S., DeWitt, D.P., 2011. Fundamentals of heat and mass transfer. John Wiley & Sons.

Broday, D.M., Georgopoulos, P.G., 2001. Growth and deposition of hygroscopic particulate matter in the human lungs. Aerosol Science & Technology 34, 144–159.

Brouns, M., Verbanck, S., Lacor, C., 2007. Influence of glottic aperture on the tracheal flow. Journal of Biomechanics 40, 165–172.

Burden, R., Faires, J., 2010. Numerical Analysis. Brooks/Cole Cengage Learning.

Carey, G., Finlayson, B.A., 1975. Orthogonal collocation on finite elements. Chemical Engineering Science 30, 587–596.

Chan, H., Phipps, P., Gonda, I., Cook, P., Fulton, R., Young, I., Bautovich, G., 1994. Regional deposition of nebulized hypodense nonisotonic solutions in the human respiratory tract. European Respiratory Journal 7, 1483–1489.

Chan, T., Lippmann, M., 1980. Experimental measurements and empirical modeling of the regional deposition of inhaled particles in humans. American Industrial Hygiene Association Journal 41, 399–408.

Chandrasekhar, S., 1943. Stochastic problems in physics and astronomy. Reviews of modern physics 15, 1–89.

Chen, C., Levine, S., 1973. The double-layer interaction of two charged colloidal spherical particles of a concentrated dispersion in a medium of low dielectric constant: I. force calculations. Journal of Colloid and Interface Science 43, 599–615.

Cheng, Y.S., 2003. Aerosol deposition in the extrathoracic region. Aerosol Science & Technology 37, 659–671.

Cheng, Y.S., Smith, S.M., Yeh, H.C., Kim, D.B., Cheng, K.H., Swift, D.L., 1995. Deposition of ultrafine aerosols and thoron progeny in replicas of nasal airways of young children. Aerosol Science & Technology 23, 541–552.

Cinkotai, F., 1971. The behaviour of sodium chloride particles in moist air. Journal of Aerosol Science 2, 325–329.

Coates, M.S., Chan, H.K., Fletcher, D.F., Chiou, H., 2007. Influence of mouthpiece geometry on the aerosol delivery performance of a dry powder inhaler. Pharmaceutical Research 24, 1450–1456.

Cohen, S., Hindmarsh, A., 1994. CVODE User Guide. Technical Report. Lawrence Livermore National Laboratory, Numerical Mathematics Group.

Conway, J., Fleming, J., Majoral, C., Katz, I., Perchet, D., Peebles, C., Tossici-Bolt, L., Collier, L., Caillibotte, G., Pichelin, M., et al., 2012. Controlled, parametric, individualized, 2-d and 3-d imaging measurements of aerosol deposition in the respiratory tract of healthy human subjects for model validation. Journal of Aerosol Science 52, 1–17.

Corcoran, T., Gamard, S., 2004. Development of aerosol drug delivery with helium oxygen gas mixtures. Journal of Aerosol Medicine 17, 299–309.

Corcoran, T.E., Shortall, B.P., Kim, I.K., Meza, M.P., Chigier, N., 2003. Aerosol drug delivery using heliox and nebulizer reservoirs: results from an mri-based pediatric model. Journal of Aerosol Medicine 16, 263–271.

Darquenne, C., Prisk, G.K., 2004. Aerosol deposition in the human respiratory tract breathing air and 80: 20 heliox. Journal of Aerosol Medicine 17, 278–285.

Daviskas, E., Gonda, I., Anderson, S.D., 1990. Mathematical modeling of heat and water transport in human respiratory tract. Journal of Applied Physiology 69, 362–372.

De Boor, C., Swartz, B., 1973. Collocation at Gaussian points. SIAM Journal on Numerical Analysis 10, 582–606.

DeHaan, W.H., Finlay, W.H., 2001. In vitro monodisperse aerosol deposition in a mouth and throat with six different inhalation devices. Journal of Aerosol Medicine 14, 361–367.

Derjaguin, B., Landau, L., 1941. Theory of the stability of strongly charged lyophobic sols and of the adhesion of strongly charged particles in solution of electrolytes. Acta Physicochimica: USSR 14, 633–662.

Dhand, R., 2004. Basic techniques for aerosol delivery during mechanical ventilation. Respiratory Care 49, 611–622.

Douglas, J., Dupont, T., 1973. A finite element collocation method for quasilinear parabolic equations. Mathematics of Computation 27, 17–28.

Elkins, M.R., Bye, P.T., 2006. Inhaled hypertonic saline as a therapy for cystic fibrosis. Current opinion in pulmonary medicine 12, 445–452.

Féat, G., Levine, S., 1975. Double-layer interaction of two charged colloidal spherical particles of a concentrated dispersion in a medium of low dielectric constant: II. a cell model. Journal of the Chemical Society, Faraday Transactions 2: Molecular and Chemical Physics 71, 102–118.

Féat, G., Levine, S., 1976. The double-layer interaction of two charged colloidal spherical particles of a concentrated dispersion in a medium of low dielectric constant: III. approximation of perfectly conducting particles. Journal of Colloid and Interface Science 54, 34–44.

Ferron, G., Haider, B., Kreyling, W., 1988-a. Inhalation of salt aerosol particles i. estimation of the temperature and relative humidity of the air in the human upper airways. Journal of Aerosol Science 19, 343–363.

Ferron, G., Kreyling, W., Haider, B., 1988-b. Inhalation of salt aerosol particles ii. growth and deposition in the human respiratory tract. Journal of Aerosol Science 19, 611–631.

Finlay, W., Stapleton, K., 1995. The effect on regional lung deposition of coupled heat and mass transfer between hygroscopic droplets and their surrounding phase. Journal of aerosol science 26, 655–670.

Finlay, W., Stapleton, K., Chan, H., Zuberbuhler, P., Gonda, I., 1996. Regional deposition of inhaled hygroscopic aerosols: in vivo spect compared with mathematical modeling. Journal of Applied Physiology 81, 374–383.

Finlay, W.H., 1998. Estimating the type of hygroscopic behavior exhibited by aqueous droplets. Journal of Aerosol Medicine 11, 221–229.

Finlay, W.H., 2001. The mechanics of inhaled pharmaceutical aerosols: an introduction. Academic Press.

Finlay, W.H., Lange, C.F., King, M., Speert, D.P., 2000. Lung delivery of aerosolized dextran. American Journal of Respiratory and Critical Care Medicine 161, 91–97.

Friedlander, S.K., 2000. Smoke, Dust, and Haze: Fundamentals of Aerosol Dynamics. 2 ed., Oxford University Press, New York.

Fuchs, N., 1959. Evaporation and droplet growth in gaseous media. Pergamon.

Garcia, G.J., Tewksbury, E.W., Wong, B.A., Kimbell, J.S., 2009. Interindividual variability in nasal filtration as a function of nasal cavity geometry. Journal of Aerosol Medicine and Pulmonary Drug Delivery 22, 139–156.

Gelbard, F., 1979. The general dynamic equation for aerosols. Ph.D. thesis. California Institute of Technology.

Gelbard, F., Seinfeld, J.H., 1978. Numerical solution of the dynamic equation for particulate systems. Journal of Computational Physics 28, 357–375.

Gelbard, F., Seinfeld, J.H., 1979. The general dynamic equation for aerosols. theory and application to aerosol formation and growth. Journal of Colloid and Interface Science 68, 363–382.

Gelbard, F., Tambour, Y., Seinfeld, J.H., 1980. Sectional representations for simulating aerosol dynamics. Journal of Colloid and Interface Science 76, 541–556.

Gemci, T., Shortall, B., Allen, G., Corcoran, T., Chigier, N., 2003. A CFD study of the throat during aerosol drug delivery using heliox and air. Journal of Aerosol Science 34, 1175–1192.

Golshahi, L., Finlay, W., 2012. An idealized child throat that mimics average pediatric oropharyngeal deposition. Aerosol Science and Technology 46, i–iv.

Golshahi, L., Finlay, W., Olfert, J., Thompson, R., Noga, M., 2010. Deposition of inhaled ultrafine aerosols in replicas of nasal airways of infants. Aerosol Science and Technology 44, 741–752.

Golshahi, L., Noga, M., Thompson, R., Finlay, W., 2011. In vitro deposition measurement of inhaled micrometer-sized particles in extrathoracic airways of children and adolescents during nose breathing. Journal of Aerosol Science 42, 474–488.

Golshahi, L., Noga, M., Vehring, R., Finlay, W., 2013. An in vitro study on the deposition of micrometer-sized particles in the extrathoracic airways of adults during tidal oral breathing. Annals of Biomedical Engineering 41, 979–989.

Goode, M.L., Fink, J.B., Dhand, R., Tobin, M.J., 2001. Improvement in aerosol delivery with helium–oxygen mixtures during mechanical ventilation. American Journal of Respiratory and Critical Care Medicine 163, 109–114.

Grgic, B., Finlay, W., Burnell, P., Heenan, A., 2004a. In vitro intersubject and intrasubject deposition measurements in realistic mouth–throat geometries. Journal of Aerosol Science 35, 1025–1040.

Grgic, B., Finlay, W., Heenan, A., 2004b. Regional aerosol deposition and flow measurements in an idealized mouth and throat. Journal of Aerosol Science 35, 21–32.

Habib, D.M., Garner, S.S., Brandeburg, S., 1999. Effect of helium-oxygen on delivery of albuterol in a pediatric, volume-cycled, ventilated lung model. Pharmacotherapy: The Journal of Human Pharmacology and Drug Therapy 19, 143–149.

Hahn, I., Scherer, P.W., Mozell, M.M., 1993. Velocity profiles measured for airflow through a large-scale model of the human nasal cavity. Journal of Applied Physiology 75, 2273–2287.

Heenan, A., Matida, E., Pollard, A., Finlay, W., 2003. Experimental measurements and computational modeling of the flow field in an idealized human oropharynx. Experiments in Fluids 35, 70–84.

Heyder, J., 1975. Gravitational deposition of aerosol particles within a system of randomly oriented tubes. Journal of Aerosol Science 6, 133–137.

Heyder, J., Gebhart, J., 1977. Gravitational deposition of particles from laminar aerosol flow through inclined circular tubes. Journal of Aerosol Science 8, 289–295.

Hickey, A., Evans, R., 1996. Aerosol generation from propellant-driven metered dose inhalers. Lung Biology in Health and Disease 94, 417–439.

Hindle, M., Longest, P.W., 2010. Evaluation of enhanced condensational growth (ECG) for controlled respiratory drug delivery in a mouth-throat and upper tracheobronchial model. Pharmaceutical research 27, 1800–1811.

Hindle, M., Longest, P.W., 2012. Condensational growth of combination drug-excipient submicrometer particles for targeted high-efficiency pulmonary delivery: evaluation of formulation and delivery device. Journal of Pharmacy and Pharmacology 64, 1254–1263.

Hounam, R., Black, A., Walsh, M., 1971. The deposition of aerosol particles in the nasopharyngeal region of the human respiratory tract. Journal of Aerosol Science 2, 47–61.

Ingham, D., 1975. Diffusion of aerosols from a stream flowing through a cylindrical tube. Journal of Aerosol Science 6, 125–132.

Jacobson, M.Z., 2005. Fundamentals of atmospheric modeling. Cambridge University Press.

Janssens, H.M., de Jongste, J.C., Fokkens, W.J., Robben, S.G., Wouters, K., Tiddens, H.A., 2001. The sophia anatomical infant nose-throat (saint) model: a valuable tool to study aerosol deposition in infants. Journal of Aerosol Medicine 14, 433–441.

Jarvis, P., Jefferson, B., Parsons, S.A., 2005. Measuring floc structural characteristics. Reviews in Environmental Science and Bio Technology 4, 1–18.

Javaheri, E., Finlay, W.H., 2013. Size manipulation of hygroscopic saline droplets: Application to respiratory drug delivery. International Journal of Heat and Mass Transfer 67, 690–695.

Javaheri, E., Finlay, W.H., 2014. Numerical simulation of flocculation and transport of suspended particles: Application to metered-dose inhalers. International Journal of Multiphase Flow 64, 28–34.

Javaheri, E., Golshahi, L., Finlay, W., 2013a. An idealized geometry that mimics average infant nasal airway deposition. Journal of Aerosol Science 55, 137–148.

Javaheri, E., Shemirani, F.M., Pichelin, M., Katz, I.M., Caillibotte, G., Vehring, R., Finlay, W.H., 2013b. Deposition modeling of hygroscopic saline aerosols in the human respiratory tract: Comparison between air and helium–oxygen as carrier gases. Journal of Aerosol Science 64, 81–93.

Jensen, M.K., 1989. Simultaneously developing laminar flow in an isothermal circular tube. International Communications in Heat and Mass Transfer 16, 811–820.

Jin, H., Fan, J., Zeng, M., Cen, K., 2007. Large eddy simulation of inhaled particle deposition within the human upper respiratory tract. Journal of Aerosol Science 38, 257–268.

Johnson, K.A., 1996. Interfacial phenomena and phase behavior in metered dose inhaler formulations. Lung Biology in Health and Disease 94, 385–415.

Katz, I., Caillibotte, G., Martin, A.R., Arpentinier, P., 2011. Property value estimation for inhaled therapeutic binary gas mixtures: He, Xe, N_2O, and N_2 with O_2. Medical Gas Research , 1–28.

Kelly, J.T., Asgharian, B., Kimbell, J.S., Wong, B.A., 2004. Particle deposition in human nasal airway replicas manufactured by different methods. part i: Inertial regime particles. Aerosol Science and Technology 38, 1063–1071.

Keyhani, K., Mozell, M., Scherer, P., 1995. Numerical simulation of airflow in the human nasal cavity. Journal of Biomechanical Engineering 117, 429–441.

Kim, Y.P., Seinfeld, J.H., Saxena, P., 1993. Atmospheric gas-aerosol equilibrium i. thermodynamic model. Aerosol Science and Technology 19, 157–181.

Laube, B.L., Sharpless, G., Shermer, C., Nasir, O., Sullivan, V., Powell, K., 2010. Deposition of albuterol aerosol generated by pneumatic nebulizer in the sophia anatomical infant nose-throat (saint) model. Pharmaceutical Research 27, 1722–1729.

LeVeque, R.J., 2002. Finite volume methods for hyperbolic problems. Cambridge university press.

Liu, Y., Johnson, M.R., Matida, E.A., Kherani, S., Marsan, J., 2009. Creation of a standardized geometry of the human nasal cavity. Journal of Applied Physiology 106, 784–795.

Lombard, M., 2008. SolidWorks surfacing and complex shape modeling bible. John Wiley & Sons, Indianapolis. pp. 33–54.

Londahl, J., Massling, A., Pagels, J., Swietlicki, E., Vaclavik, E., Loft, S., 2007. Size-resolved respiratory-tract deposition of fine and ultrafine hydrophobic and hygroscopic aerosol particles during rest and exercise. Inhalation Toxicology 19, 109–116.

Longest, P.W., Hindle, M., 2010. CFD simulations of enhanced condensational growth (ECG) applied to respiratory drug delivery with comparisons to in vitro data. Journal of Aerosol Science 41, 805–820.

Longest, P.W., Hindle, M., 2011. Numerical model to characterize the size increase of combination drug and hygroscopic excipient nanoparticle aerosols. Aerosol Science and Technology 45, 884–899.

Longest, P.W., Hindle, M., 2012. Condensational growth of combination drug-excipient submicrometer particles for targeted high efficiency pulmonary delivery: comparison of CFD predictions with experimental results. Pharmaceutical research 29, 707–721.

Longest, P.W., Spence, B.M., Holbrook, L.T., Mossi, K.M., Son, Y.J., Hindle, M., 2012a. Production of inhalable submicrometer aerosols from conventional mesh nebulizers for improved respiratory drug delivery. Journal of aerosol science 51, 66–80.

Longest, P.W., Tian, G., Li, X., Son, Y.J., Hindle, M., 2012b. Performance of combination drug and hygroscopic excipient submicrometer particles from a softmist inhaler in a characteristic model of the airways. Annals of biomedical engineering 40, 2596–2610.

Longest, P.W., Walenga, R.L., Son, Y.J., Hindle, M., 2013. High-efficiency generation and delivery of aerosols through nasal cannula during noninvasive ventilation. Journal of aerosol medicine and pulmonary drug delivery .

Longest, P.W., Xi, J., 2008. Condensational growth may contribute to the enhanced deposition of cigarette smoke particles in the upper respiratory tract. Aerosol Science & Technology 42, 579–602.

Marieb, E.N., Hoehn, K., 2007. Human anatomy & physiology. Pearson Education.

Martonen, T., 1982. Analytical model of hygroscopic particle behavior in human airways. Bulletin of Mathematical Biology 44, 425–442.

Mason, B., 2010. The Physics of Clouds. Oxford University Press.

Mitchell, J.P., 2008. Appropriate face models for evaluating drug delivery in the laboratory: The current situation and prospects for future advances. Journal of Aerosol Medicine and Pulmonary Drug Delivery 21, 97–112.

Mitsakou, C., Mitrakos, D., Neofytou, P., Housiadas, C., 2007. A simple mechanistic model of deposition of water-soluble aerosol particles in the mouth and throat. Journal of Aerosol Medicine 20, 519–529.

Miyawaki, S., Tawhai, M.H., Hoffman, E.A., Lin, C.L., 2012. Effect of carrier gas properties on aerosol distribution in a ct-based human airway numerical model. Annals of Biomedical Engineering 40, 1495–1507.

Morrow, P.E., Bates, D., Fish, B., Hatch, T., Mercer, T., 1966. Deposition and retention models for internal dosimetry of the human respiratory tract. Health Physics 12, 173–207.

Nerbrink, O., Dahlbäck, M., 1994. Basic nebulizer function. Journal of Aerosol Medicine 7, 7–11.

O'Callaghan, C., Barry, P.W., 1997. The science of nebulised drug delivery. Thorax 52, 31.

Patankar, S.V., 1980. Numerical heat transfer and fluid flow. Taylor & Francis.

Persons, D.D., Hess, G.D., Muller, W.J., Scherer, P.W., 1987. Airway deposition of hygroscopic heterodispersed aerosols: results of a computer calculation. Journal of Applied Physiology 63, 1195–1204.

Peterson, J.B., Prisk, G.K., Darquenne, C., 2008. Aerosol deposition in the human lung periphery is increased by reduced-density gas breathing. Journal of Aerosol Medicine and Pulmonary Drug Delivery 21, 159–168.

Phalen, R.F., Oldham, M.J., 2001. Methods for modeling particle deposition as a function of age. Respiration Physiology 128, 119–130.

Phipps, P.R., Gonda, I., 1994. Evaporation of aqueous aerosols produced by jet nebulizers: effects on particle size and concentration of solution in the droplets. Journal of Aerosol Medicine 7, 239–258.

Proctor, D.F., Andersen, I.H.P., 1982. The nose, upper airway physiology and the atmospheric environment. Elsevier Biomedical Press, New York. pp. 23–43.

Reid, R.C., Prausnitz, J.M., Poling, B.E., 1987. The properties of gases and liquids. McGraw Hill, New York.

Russel, W.B., Saville, D.A., Schowalter, W.R., 1992. Colloidal dispersions. Cambridge university press.

Saleh, R., Shihadeh, A., 2007. Hygroscopic growth and evaporation in an aerosol with boundary heat and mass transfer. Journal of aerosol science 38, 1–16.

Sandeau, J., Katz, I., Fodil, R., Louis, B., Apiou-Sbirlea, G., Caillibotte, G., Isabey, D., 2010. CFD simulation of particle deposition in a reconstructed human oral extrathoracic airway for air and helium–oxygen mixtures. Journal of Aerosol Science 41, 281–294.

Sasaki, C.T., Levine, P.A., Laitman, J.T., Crelin, E.S., 1977. Postnatal descent of the epiglottis in man: a preliminary report. Archives of Otolaryngology 103, 169–171.

Schreck, S., Sullivan, K., Ho, C., Chang, H., 1993. Correlations between flow resistance and geometry in a model of the human nose. Journal of Applied Physiology 75, 1767–1775.

Schroeter, J.D., Garcia, G.J., Kimbell, J.S., 2011. Effects of surface smoothness on inertial particle deposition in human nasal models. Journal of Aerosol Science 42, 52–63.

Scott, W.T., 1968. Analytic studies of cloud droplet coalescence. Journal of Atmospheric Science 25, 54–65.

Seinfeld, J.H., Pandis, S.N., 2006. Atmospheric chemistry and physics: from air pollution to climate change. Wiley-Interscience.

Stahlhofen, W., Rudolf, G., James, A., 1989. Intercomparison of experimental regional aerosol deposition data. Journal of Aerosol Medicine 2, 285–308.

Stapleton, K., Finlay, W., 1995. Determining solution concentration within aerosol droplets output by jet nebulizers. Journal of aerosol science 26, 137–145.

Stapleton, K., Finlay, W., 1997. Deposition of medical aerosols in the human respiratory tract. report ma-1. Department of Mechanical Engineering, University of Alberta, Edmonton, Alberta, Canada .

Stapleton, K., Finlay, W., Zuberbuhler, P., 1994. An in vitro method for determining regional dosages delivered by jet nebulizers. Journal of aerosol medicine 7, 325–344.

Stapleton, K., Guentsch, E., Hoskinson, M., Finlay, W., 2000. On the suitability of k-epsilon turbulence modeling for aerosol deposition in the mouth and throat: a comparison with experiment. Journal of Aerosol Science 31, 739–749.

Storey-Bishoff, J., Noga, M., Finlay, W., 2008. Deposition of micrometer-sized aerosol particles in infant nasal airway replicas. Journal of Aerosol Science 39, 1055–1065.

Svartengren, M., Anderson, M., Philipson, K., Camner, P., 1989. Human lung deposition of particles suspended in air or in helium–oxygen mixture. Experimental Lung Research 15, 575–585.

Swift, D., 1991. Inspiratory inertial deposition of aerosols in human nasal airway replicate casts: implication for the proposed ncrp lung model. Radiation Protection Dosimetry 38, 29–34.

Tadros, T.F., 2012. Dispersion of powders in liquids and stabilization of suspensions. John Wiley & Sons.

Verwey, E., Overbeek, J., 1948. Theory of the stability of lyophobic colloids.

Wang, Z., Grgic, B., Finlay, W., 2006. A dry powder inhaler with reduced mouth-throat deposition. Journal of Aerosol Medicine 19, 168–174.

Whitby, E.R., McMurry, P.H., 1997. Modal aerosol dynamics modeling. Aerosol Science & Technology 27, 673–688.

Williams, M.M.R., Loyalka, S.K., 1991. Aerosol Science Theory and Practice: with special applications to the nuclear industry. Pergamon.

Yu, C., Diu, C., Soong, T., 1981. Statistical analysis of aerosol deposition in nose and mouth. The American Industrial Hygiene Association Journal 42, 726–733.

Zhang, Y., Gilbertson, K., Finlay, W.H., 2007. In vivo-in vitro comparison of deposition in three mouth-throat models with Qvar and Turbuhaler inhalers. Journal of Aerosol Medicine 20, 227–235.

Zhang, Y., Seigneur, C., Seinfeld, J.H., Jacobson, M.Z., Binkowski, F.S., 1999. Simulation of aerosol dynamics: A comparative review of algorithms used in air quality models. Aerosol Science & Technology 31, 487–514.

Zhou, Y., Sun, J., Cheng, Y.S., 2011. Comparison of deposition in the usp and physical mouth–throat models with solid and liquid particles. Journal of Aerosol Medicine and Pulmonary Drug Delivery 24, 277–284.